Plasma Physics and
Controlled Fusion

PAPER • OPEN ACCESS

Nanofoam in action: a versatile tool for laser-plasma interaction experiments

To cite this article: Alessandro Maffini *et al* 2026 *Plasma Phys. Control. Fusion* **68** 035007

IOP Publishing Plasma Phys. Control. Fusion **68** (2026) 035007 https://doi.org/10.1088/1361-6587/ae44c8

Plasma Physics and Controlled Fusion

OPEN ACCESS

RECEIVED
30 October 2025

REVISED
10 January 2026

ACCEPTED FOR PUBLICATION
11 February 2026

PUBLISHED
3 March 2026

PAPER

Nanofoam in action: a versatile tool for laser-plasma interaction experiments

Alessandro Maffini[1,*], Kevin Ambrogioni[1], David Dellasega[1], Marta Galbiati[1,2], Maria Sole Galli de Magistris[1], Francesco Gatti[1,5], Matteo Iaccarino[1,3], Claudia Mallimaci[1,4], Francesco Mirani[1], Davide Orecchia[1], Valeria Russo[1], Davide Vavassori[1] and Matteo Passoni[1]

[1] Dipartimento di Energia, Politecnico di Milano, Milan, Italy
[2] Laboratoire pour l'Utilisation des Lasers Intenses (LULI), CNRS, CEA, Sorbonne Université, École Polytechnique, Institut Polytechnique de Paris, F-91128 Palaiseau, France
[3] ELI Beamlines Facility, The Extreme Light Infrastructure ERIC, Dolní Břežany, Czech Republic
[4] Nuclear Department, ENEA, C.R. Frascati, Frascati, Italy
[5] Current address: European XFEL, Schenefeld 22869, Germany
[*] Author to whom any correspondence should be addressed.

E-mail: alessandro.maffini@polimi.it

Keywords: nanofoam, near-critical target, pulsed laser deposition, laser-plasma interaction, TNSA, direct drive ICF, proton-boron fusion

Supplementary material for this article is available online

Abstract

Low-density near-critical materials in laser-plasma interaction (LPI) stand out for their capability in enhancing the coupling between the laser radiation and the target. Indeed, they can be exploited for fundamental physics studies, optimised particle acceleration for practical applications, and inertial confinement fusion. However, the modelling of complex non-linear phenomena occurring during the interaction of these materials and high-intensity lasers, together with the accurate control and characterisation of their physical properties, are still object of intense research. In this context, near-critical nanofoams produced via pulsed laser deposition represent a promising option owing to the versatility and controllability of their deposition technique. In this paper, we report on our modelling and experimental activities related to laser-nanofoam interaction. In particular, we first present the deposition methodology, focusing on the production of nanofoams with controlled composition and morphology. Then, we show our numerical strategy to model the foam aggregation. We also discuss how the nanofoam morphology affects the LPI by integrating the realistic nanostructure in particle-in-cell simulations, focusing on various regimes of interaction. Lastly, we present examples of applications of nanofoam-based targets via numerical simulations and experiments, focusing also on the open issues for reaching the requirements for full-fledged applications. Our work demonstrates nanofoam-based targets as a versatile tool to effectively optimise and advance LPI physics.

1. Introduction

Nanofoams are porous, nanostructured materials with a very large fraction of sub-micrometric voids and a disordered, fractal-like backbone of nanoparticles. Their typical density spans 1-100 $\mathrm{mg\,cm^{-3}}$, and they offer a high surface-to-volume ratio. These features have drawn interest across many research areas such as hydrogen storage [1], next generation supercapacitors [2] and catalysts [3], water purification [4], CO_2 capture and storage [5], and nano-medicine [6]. In the context of high-intensity laser-plasma interaction (LPI), low-density and near-critical media enable stronger laser-target coupling than homogeneous, bulk-density solids, allowing for efficient absorption from femtosecond to nanosecond regimes [7, 8].

Depending on their properties in terms of density, thickness, and nanostructure, nanofoams can shape the plasma profile seen by a super-intense laser pulse and hence control the whole process of

LPI [7]. In the relativistic, ultrashort-pulse limit, nanofoams enhance the heating and acceleration of the electron population [9–13], which, in turn, drives the generation of high-energy photons [14–17] and the acceleration of light ions via the target normal sheath acceleration (TNSA) [18, 19]. In longer, nanosecond interactions, scattering and deep penetration of the laser field through the void network favour volumetric heating and homogenisation dynamics. This affects the growth of instabilities and the propagation of shock waves, crucial issues in the field of inertial confinement fusion (ICF) [20, 21] and high-energy-density physics [22].

Nanofoam structures naturally arise when ultrashort lasers interact with solid matter, effect observed for a variety of materials irradiated with high repetition rate (kHz–MHz) low energy pulses (∼mJ) [23–25]. This behaviour opens the interesting possibility of in-situ laser structuring and nanofoam formation during high-intensity LPI experiments. Indeed, analogous approaches have been successfully demonstrated for simpler nanostructuring strategies, such as LIPSS surface structuring [26, 27]. In contrast, nanofoams present additional challenges: the complexity of their growth mechanism and laser-matter interaction behaviour, leading to the necessity for improved material properties control, and the potential contradicting requirements between nanofoam and underlying solid substrate, such as different composition or the need of a sub-micrometric substrate (at odds with the requirements for in-situ structuring).

Among the different methods proposed to synthesise nanofoams, pulsed-laser deposition (PLD) [28, 29] has emerged as a versatile tool to grow nanofoams with controlled morphology on different kinds of substrates. Thanks to its features and flexibility, PLD represents an ideal tool to fabricate targets for LPI experiments. The nanofoam density can be tuned over a wide range, from solid density down to near-critical values ($n_\mathrm{c} = m_\mathrm{e}\epsilon_0\omega^2/e^2$, where m_e is the electron mass, ϵ_0 is the electric permittivity in vacuum, and ω is the electromagnetic radiation angular frequency), while keeping a nanostructure made of sub-wavelength building blocks, namely nanoparticles assembled in micrometric aggregates. In parallel, PLD offers precise control of elemental composition, including single-element and mixed systems made by sequential or co-deposition [28]. This combination of LPI-relevant parameters (density, nanostructure, composition) can be adjusted by suitably acting on the deposition parameters, such as pulse duration and fluence, working gas pressure, and deposition geometry.

Such control is key for double-layer targets (DLTs), where a near-critical nanofoam is put in front of a micrometric foil. The nanofoam improves laser coupling and hot-electron generation; hot electrons, then, either convert their energy directly into high-energy photons or build strong longitudinal fields through charge separation, boosting ion acceleration via enhanced TNSA. Experiments and simulations have shown higher proton energies/flux and increased bremsstrahlung with DLTs, consistent with this picture [16, 30, 31]. PLD nanofoams are also attractive for fusion. As ablators in direct-drive ICF, carbon nanofoams can raise the shock pressure, pointing to better ablation loading and smoother drive [32]. In proton-boron schemes, PLD enables the production of boron- and hydrogen-rich nanofoams, either stacked or mixed, that have demonstrated relevant α-particle yields.

In this paper, we present a review of our most relevant contributions to this field, together with new results concerning PLD nanofoam production for LPI, numerical investigation of LPI with nanofoams, and their applications, including DLT-enabled enhanced TNSA, high-energy photon and neutron sources, radioisotope generation, materials characterisation and fusion-relevant targets. In particular, in section 2 we summarise how we produce and characterise PLD nanofoams and related substrates for DLTs, highlighting process knobs and morphology-density control. We also present modelling strategies for PLD nanofoam growth. We, then, discuss laser-nanofoam interaction on ultrashort and nanosecond time scales (section 3), linking absorption, electron heating, and shock formation to foam density and structure. Next, we focus on DLTs: we show how near-critical foams on micrometric foils boost TNSA and support high-energy photon and particle generation (gamma and positrons), and we report open issues relevant to reliable operation, e.g. foam damage in proximity of the taken laser shot and differences observed across facilities (section 4). Building on these results, we assess application-oriented sources at fixed laser parameters, comparing solid foils and DLTs for applications such as neutron generation, radioisotope yields (e.g. ^{11}C), and full-field particle-induced x-ray emission (FF-PIXE) elemental mapping (section 5). Lastly, we review the role of nanofoams in laser-driven fusion, from boron- and hydrogen-rich foams for p-^{11}B schemes to carbon nanofoams as advanced ablators for ICF (section 6). Across these sections, we aim to provide a unified picture of ‘nanofoam in action’: from PLD growth and scaling laws to interaction physics and application performance. Where possible, we combine simulations and experiments already reported in the literature to substantiate our results (e.g. neutron sources and radioisotopes with DLTs), and we point out practical constraints for high-repetition-rate use (namely, prepulse sensitivity and target integrity after shooting). We conclude by outlining some open questions (e.g. new development in PLD, extending modelling beyond sub-ps dynamics, integrating nanoscale structure in ICF-relevant frameworks), which, if addressed, can turn nanofoams into a practical and robust tool for enhancing high-intensity LPI.

2. Production and characterisation of nanofoam targets

In LPI, the target plays a crucial role. Its properties, including morphology, density, thickness and composition, strongly affect the laser-target coupling and the interaction physics. Therefore, target characteristics should be tailored to specific laser parameters and the application of interest. In this section, we highlight nanofoam properties can be controlled by exploiting the versatility of PLD. We also describe how foam characteristics can be predicted via scaling laws, which also enables the simulation of their growth numerically. Additionally, we present the deposition strategies for the production of carbon nanofoams, employed as near-critical layer in DLTs, for the production of hydrogen-rich nanofoams for laser-driven p-B fusion, and the development of free-standing metallic foils to be employed as solid layers in DLTs.

2.1. Foams for high-power laser-matter interaction experiments

Foam's properties depend on the synthesis route, which determines both the material composition, and the resulting morphology and density. Three main families of fabrication approaches can be distinguished: chemical synthesis, additive manufacturing, and physical processes. Chemical methods are widely employed because of their relative simplicity. These include templating techniques [33–35], block copolymer self-assembly [36, 37], and direct synthesis approaches [36]. However, they present some limitations: each method is generally restricted to specific classes of materials, not all of them allow for structuring at the nano-scale, control over the morphology is usually limited, and in some cases, toxic reagents or by-products are involved. Additive manufacturing methods [38] offer flexibility in tailoring foam morphology, enabling control over pore shape and size, which is, however, in the order of tens to hundreds of micrometres, making nanostructuring difficult. Physical processes, such as PLD [39], supercritical-drying [40, 41] and freeze-drying methods [40, 42], can provide superior control over foam properties, while reducing issues related to chemical toxicity. Nevertheless, their complexity limits their widespread use for foam production.

The nanofoams of interest for this work are produced via PLD, a physical vapour deposition technique that has emerged as a versatile tool to grow nanofoams with controlled morphology on different kinds of substrates. In PLD, a laser pulse ablates a solid target; the ablated species expand in a background gas and can assemble into aggregates that deposit on a substrate [39, 43, 44].

PLD nanofoams are built from nanoparticles that assemble into micrometric, fractal-like aggregates. Nanoscale features of the nanofoams (i.e. nanoparticle size, aggregate gyration radius, and fractal dimension) can be linked through a simple scaling law to macroscopic properties such as average density and uniformity. These relations enable predictive control of foam density and morphology by acting on the deposition parameters, such as pulse duration, fluence, working gas pressure, and geometry. Concerning laser pulse duration, two ablation regimes can be exploited: conventional nanosecond PLD (ns-PLD), dominated by thermal ablation [45], and femtosecond PLD (fs-PLD), where ablation is driven by a non-thermal electron population [46], possibly leading to the direct ejection of atomic clusters and nanoparticles. Not requiring heating and melting of the target, fs-PLD is suitable for the production of nanofoams of a wide variety of materials.

Another relevant parameter is the working gas pressure. A sufficiently high background pressure can slow the ablated species to a diffusive regime, promoting their aggregation while in flight, before reaching the substrate. Therefore, by properly tuning the working gas pressure, the density and structure of the nanofoam can be controlled [39]. Due to its versatility, PLD allows for nanostructuring, morphological control, density tunability (from near-bulk density down to tens of $\mathrm{mg\,cm^{-3}}$, depending on the material), and high flexibility in materials choice [44].

Figure 1 reports morphologies and densities of nanofoams and nanostructured films of different materials produced via fs-PLD and ns-PLD. In all cases, the density decreases with increasing pressure, following a sigmoidal function in logarithmic scale as shown in the plot of figure 1:

$$\rho\left(P\right) = \rho_0 \left(\frac{\rho_f}{\rho_0}\right)^{\left[\frac{P^k}{P^k + P_0^k}\right]}, \tag{1}$$

being $\rho(P)$ the film mean density as a function of pressure P, ρ_0 the compact film density, ρ_f the minimum foam density achievable with the deposited material, P_0 the centre of the sigmoid, where a sharp variation in density occurs, and k a parameter which measures the gradient of this transition [44].

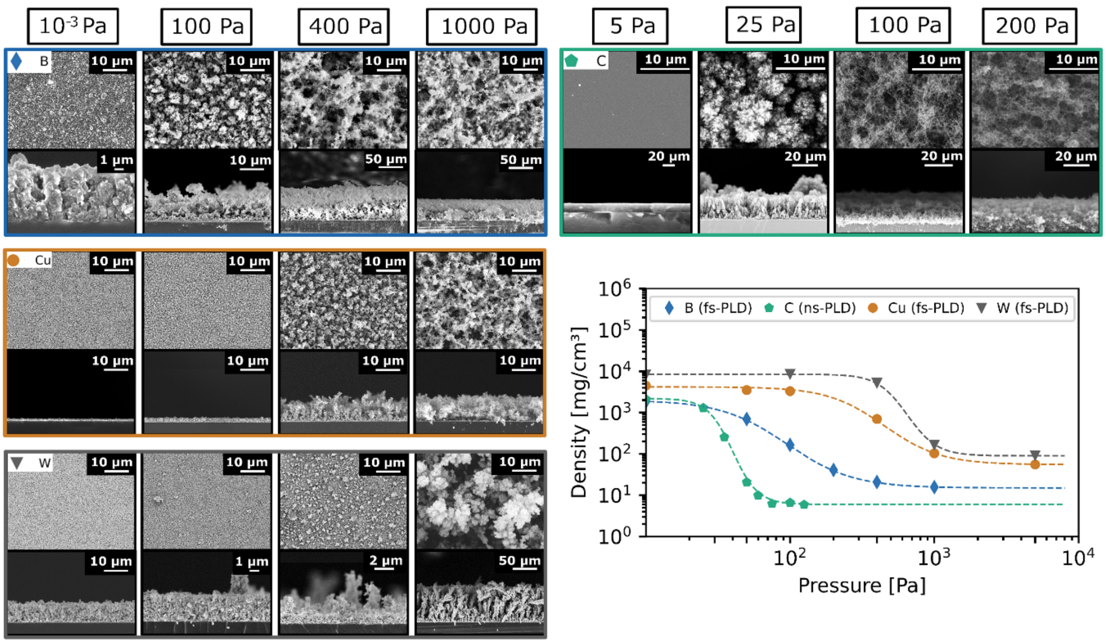

Figure 1. SEM images of nanostructured coatings of different materials produced via fs-PLD (B, Cu, (W) and ns-PLD (C). Samples were produced at different background pressures to show the effect on the density. The experimental density values are plotted and fitted with a log-log sigmoidal function, valid for every material and ablation regime, provided the optimal fitting parameters are chosen.

The main differences between the ns-PLD and the fs-PLD techniques for nanofoam growth have been discussed in detail in a previous work on carbon nanofoams [39] and extended to other elements in a study focused on fs-PLD [44]. Carbon is somewhat unique among target materials because it does not feature a thermodynamically stable liquid phase at ambient pressure; this has implications for the balance between melting, fragmentation and direct nanoparticle ejection during laser ablation. As a consequence, both deposition regimes produce carbon nanofoams composed of fractal aggregates of similar fractal dimension made of nanoparticles of comparable size, and the growth can be described by the same in-flight cluster-cluster aggregation process. Nevertheless, the background gas pressure affects differently the average nanofoam density, and at the same average density ns-PLD tends to yield more uniform sponge-like structures whereas fs-PLD produces more open, web-like morphologies. Beyond carbon, fs-PLD has been shown to lead to the direct synthesis of nanoparticles for all investigated elements [44], which then aggregate in the background gas to form nanofoams. This makes fs-PLD a very versatile tool for the fabrication of nanofoams with different elemental compositions, including multi-element and composite systems obtained by co-deposition or sequential deposition. From a practical point of view, ns-laser systems are generally simpler to operate and more widely available than high-energy fs systems, therefore ns-PLD represents a natural workhorse for the production of carbon nanofoams when uniform near-critical layers or ablators are required. Conversely, when nanofoams of other materials are needed, or when flexibility in composition is essential (e.g. hydrogen-rich polymers or multi-component nanofoams for nuclear applications) the versatility of fs-PLD is highly desirable.

Since foam density is a crucial parameter in laser-matter interaction, being able to experimentally measure it is of paramount importance. We have developed a reference-free method to evaluate the film density and composition via scanning electron microscopy (SEM) and energy-dispersive x-ray spectroscopy (EDX), as described by Pazzaglia *et al* [47]. With this approach, densities down to a few mg cm^{-3} can be measured with errors in the order of 2–20 $\mu\mathrm{g\,cm}^{-3}$, comparable to those obtained with more demanding techniques like Rutherford backscattering spectrometry and elastic recoil detection analysis. PLD nanofoams can be exploited to probe different laser-matter interaction phenomena, relying on PLD versatility to suitably tailor density and composition according to the laser parameters and experimental aim. Here, we report on the production of two different families of nanofoam-based targets, namely carbon nanofoams and hydrogen-rich polymeric and boron nanofoams.

2.1.1. Production of carbon nanofoam-based targets via ns-PLD

Carbon nanofoams are produced exploiting a ns-PLD system equipped with a Q-switched Nd:YAG laser. Depositions are performed with the laser second harmonic ($\lambda = 532$ nm), operating at a repetition rate of 10 Hz, with a pulse length of 5–7 ns, and a fluence on target of $\sim 1\,\mathrm{J\,cm^{-2}}$. The target-to-substrate distance is 7 cm, and the substrate rotates at 11 rpm to assure good uniformity of the deposited foam. The vacuum chamber is filled with Ar (purity 99.9%), the pressure of which is regulated to tune the foam density. Specifically, at a pressure of 50 Pa and 200 Pa, densities in the order of $25\,\mathrm{mg\,cm^{-3}}$ and 6–$8\,\mathrm{mg\,cm^{-3}}$ can be obtained, respectively. The corresponding morphologies are reported in figure 1. Carbon nanofoams with a density of 6–$8\,\mathrm{mg\,cm^{-3}}$ have been widely investigated, both theoretically and experimentally, as near-critical layers in DLTs for laser-driven radiation sources (see sections 4 and 5). In this target configuration, the foam is deposited on a micrometric-thick metallic foil. Since this solid layer plays a crucial role in the TNSA process and in high-energy photon and positron generation, we have developed a method for the production of free-standing metallic foils with precisely controlled thickness and uniformity, described in section 2.3. Denser foams ($25\,\mathrm{mg\,cm^{-3}}$) can be of interest as ablation layers in ICF targets [32].

2.1.2. Production of hydrogen-rich polymeric nanofoam targets via fs-PLD

Along with the single-element films and nanofoams described above, PLD can be successfully exploited to produce films with a more complex composition, either exploiting its potential in the stoichiometric transfer of target material or considering a multiple target co-deposition approach. Polymers are not the most straightforward class of materials in this context, due to their insulating character, ensuing transparency and, generally, high ablation threshold. The most widely explored approach for polymer film deposition consists in decreasing the PLD laser wavelength to the UV range. This increase in the photon energy enables an efficient laser absorption and, thus, material ablation [48–50].

A second possibility is the exploitation of ultrashort lasers, such as in fs-PLD, where non-linear effects can overcome the low photon energy limitations, and promote ablation. In these conditions, the short pulse duration and the corresponding electronic ablation mechanism can help to reduce thermal effects such as heating and melting, which are particularly relevant in polymer film deposition for avoiding polymer degradation. In fact, if the aim is to produce polymer nanofoams with a high hydrogen content-as is the case for proton-boron fusion research, explored in section 6.1-preventing polymer alteration and the consequent hydrogen removal is fundamental. Naturally, the target polymer for deposition should be as hydrogen-rich as possible in the first place. In this work, we report the novel development of high-density polyethylene (HDPE) based targets. HDPE was chosen for its pure C-H composition and favourable thermal properties.

fs-PLD is performed by ablating an HDPE target with a Ti-Sapphire commercial laser (Coherent Astrella) providing 80-fs pulses at 800 nm, with a repetition rate of 1 kHz. The laser energy is set to 3.8 mJ, to reach a fluence on the target of $110\,\mathrm{mJ\,cm^{-2}}$ by focusing the laser to a 1.76 mm-diameter spot ($1/e^2$). The laser incidence on the target is 45°, with a proper target movement routine to ensure uniform ablation. The target-substrate distance is fixed at 3 cm. In order to obtain a porous nanofoam, the deposition chamber is filled with 5000 Pa of argon gas. Compared to the single elements of figure 1, HDPE requires a significantly higher pressure to effectively slow the ablated species to a diffusive regime. This effect is ascribable to the highly energetic ablated species expected from polymeric materials. Under these conditions, tens of micrometres of densely packed nanofoams can be produced with a density close to $120\,\mathrm{mg\,cm^{-3}}$.

Taking advantage of the versatility of fs-PLD, it is also possible to produce hydrogen-enriched versions of the single-element nanofoams of figure 1, through co-deposition with HDPE. Here, we focus on hydrogen-enriched boron nanofoams, as they are interesting for proton-boron fusion research (section 6.1). The same setup and deposition conditions outlined above for the HDPE nanofoams are exploited alongside a compound target made by combining a pure boron target with an HDPE inset. The target spiral motion enables an alternate ablation of the two components, leading to a mixed foam growth. The characteristic direct emission of nanoparticles by fs-PLD, together with the diffusive regime and cluster-cluster aggregation mechanism, results in an appropriate mixing of the two components in the nanofoam. One practical difficulty arises from the different energies of the boron and HDPE ablated species, and, thus, different argon pressures required to slow them to promote aggregation and foam growth. Increasing the pressure to match the one required by HDPE is not a viable option, since the boron nanoparticles would not be able to reach the substrate. For this reason, a pressure range compatible with boron nanofoam deposition is chosen-i.e. between 150 and 400 Pa. B-CH_2 nanofoams with a mass density between 80 and $40\,\mathrm{mg\,cm^{-3}}$ are obtained, up to $100\,\mu$m in thickness, with an adjustable ratio of boron over hydrogen depending on the size of the HDPE target inset.

2.1.3. Prospects for functional engineering of PLD nanofoams

Beyond composition, density and morphology control, PLD also offers the possibility of more advanced functional engineering of nanofoams, which we mention here as potential future developments. By switching between single-element targets, doped targets and co-deposition from different targets, one can in principle tune the elemental composition and introduce trace dopants over a wide range, as already demonstrated in other PLD-grown nanostructures such as phosphorus-doped ZnO nanowires and Si-doped Ga_2O_3 films [51, 52]. Sequential deposition and control of the fluence and background pressure would also allow for the development of graded structures, where density and composition vary along the growth direction, and where dopants are embedded in a controlled way. Such dopants could be used not only to act on the laser-target interaction, but also as built-in diagnostics. For instance, it is possible to infer plasma temperature and density with time-resolved x-ray spectroscopy [53] by adding trace metals with well separated characteristic x-ray lines to a low-Z nanofoam. Another possibility is to embed in the same target two nuclides that are meant to react in-target to enhance specific reaction channels. A systematic exploration of dopant engineering and compositional grading in PLD nanofoams for LPI and applications is left to future work.

2.2. Numerical simulation of foam growth

The numerical simulation of the nanofoam aggregation process in PLD is fundamental for both material science and plasma physics studies. Gaining insight into the aggregation process enables strategies for the optimisation of nanofoam production and leads to the possibility of accurately reproducing nanostructures in laser-nanofoam interaction simulations. In material science, Monte Carlo (MC) codes simulating Brownian motion of nanoparticles are often employed to provide an accurate description of nanomaterial aggregation, for both diffusion-limited and reaction-limited aggregation processes [54–57]. When considering the PLD process, the nanofoam growth can be described in terms of diffusion-limited aggregation. Experimental observations show that nanoparticles produced during laser-target interaction undergo a snow-like aggregation process, which is mediated by the presence of the working gas in the deposition chamber [43]. As shown in section 2.1, during this aggregation process the nanoparticles collide with the background gas and diffuse. This diffusive regime allows nanoparticles-and clusters of nanoparticles-to interact with each other, leading to the formation of larger clusters that eventually deposit onto the substrate. This cluster formation mechanism can be accurately described in terms of diffusion-limited cluster-cluster aggregation (DLCCA) models [29, 43]. The blocking exerted by already deposited clusters of nanoparticles due to their geometrical dimension, often defined as geometrical shadowing effect, is critical in the aggregation process. In fact, due to the shadowing effect, the nanofoam grows according to the cluster size, and its mean density can be related to the dimension of the clusters through a fractal scaling. The latter is described by:

$$\rho_f(N_\mathrm{P}) = k\rho_0 N_\mathrm{P}^{-\frac{3-D_\mathrm{F}}{D_\mathrm{F}}}, \qquad (2)$$

where ρ_f is the nanofoam mean density, N_P is the number of nanoparticles composing the cluster generated during the snow-like process, k is a proportionality factor, ρ_0 is the nanoparticle density, equal to the bulk one, and D_F is the fractal dimension related to the aggregation process, approximately equal to 1.8 for DLCCA [57]. This is a reasonable assumption on the basis of the snowfall-like aggregation process typical of PLD-produced nanofoam [39, 43], well-described by DLCCA. Indeed, a fractal dimension in the order of 1.8–2.0 has been obtained from experimental carbon nanofoam data [39], which is in reasonable agreement in the limits of the simulated foam approximations (i.e. fixed nanoparticle size and monodisperse N_P). This fractal scaling highlights the strong relation between the mean foam density and the morphology of the nanofoam, represented by N_P. It can be used to relate nanofoams simulated with MC codes to experimentally produced nanofoams once the aggregation process is properly described in the simulation.

In this context, we developed an MC code able to simulate the DLCCA process [17, 58]. The code proceeds in two steps. Firstly, clusters of nanoparticles are aggregated following the DLCCA process. A user-defined number of nanoparticles (N_P) is initialised and allowed to aggregate through a random walk until generating a cluster. The aggregation is performed on a 3D grid on which nanoparticles-and clusters of nanoparticles-perform a random-walk. Whenever they get a contact point, they aggregate. Then, the generated clusters are quasi-ballistically deposited onto a planar substrate, leading to the foam growth. The ballistic motion is stopped when a contact between the aggregate and already deposited particles or substrate is obtained, and the cluster is aggregated to the already deposited particles. The foam thickness is uniquely defined by the number of generated clusters (N_C). Results of the foam growth process are shown in figures 2(a) and (b), in which the cross-section and top view of a simulated

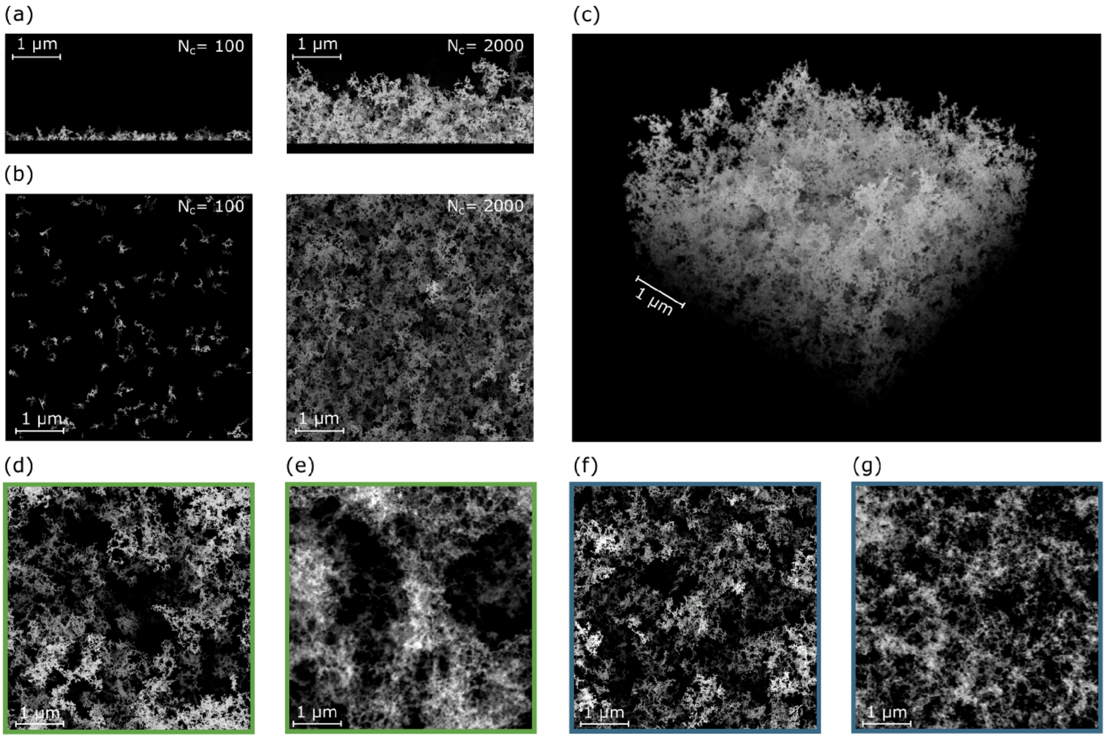

Figure 2. Simulation of nanofoam growth onto a substrate. In (a), the growth of the nanofoam onto a substrate with increasing number of clusters N_{C} is shown with a cross-section visualisation in Ovito [59]. In (b), the respective top views are presented. In (c), the 3D visualisation of the grown foam is shown. In (d), the top view of a numerically simulated web-like foam is shown to be compared with a relevant SEM image reported in (e). In (f), the top view of a numerically simulated tree-like foam is shown to be compared with a relevant SEM image reported in (g).

nanofoam are shown with increasing N_{C}, keeping constant N_{P}. Looking at the lower N_{C} (i.e. $N_C = 100$), one can observe the first steps of the nanofoam growth. During this transitory phase, the nanofoam first layers are building up: the mean density increases proportionally to N_{C}. In fact, the shadowing effect exerted by the already deposited clusters does not affect the deposition process due to the relatively small area occupied by the low number of deposited clusters, and the clusters randomly fall across the substrate. With increasing N_{C}, the geometrical shadow of the already deposited clusters becomes the limiting factor, and the foam density eventually reaches a saturation. Here, the deposited clusters create a geometrical barrier for the ones to be deposited; the latter are forced to attach to pre-deposited clusters, and the nanostructure is generated with a mean density related to the length scale of the deposited clusters. When the density saturation value is reached, the nanofoam density can be described in terms of equation (2). In figure 2(c), a 3D representation of the same foam is shown once the aggregation process is completed. The stochasticity of the process stands out from this 3D view, where the random thickness variations and voids are visible.

Here, we also present recent results on detailed comparisons between simulated and experimentally produced nanofoams at two different densities. To relate the simulated and experimental nanostructures, a quantitative characterisation is necessary. In previous works, such analysis was conducted both considering the properties of the single cluster, like the gyration radius [39], and the ones of the whole nanofoam aggregate, such as the k parameter in equation (2) [17]. Both quantities calculated in the simulated cases were found to be similar to the experimental values. Moreover, by comparing the characteristic length of the nanofoam pores estimated through a Fourier transform analysis of the mass-thickness maps similar values are obtained for the simulated and experimentally produced foams in both cases (4.5 μm and 5.5 μm for the simulated and experimental web-like foams, respectively; 1.5 μm and 2.5 μm for the simulated and experimental tree-like foams, respectively). Nevertheless, the use of a non-monodisperse distribution for N_{p} in the simulations could grant a better agreement between the characteristic length values by varying the uniformity level of the foam. The analysis of the effect of the N_{p} distribution on the simulated foam is still preliminary and will be assessed in a future work.

In Galbiati *et al* [17], we developed a method to characterise the output of the foam simulation code, enabling the simulation of realistic nanostructures given the density of the experimentally produced nanofoam. The results of this characterisation are shown in figure 2 as a comparison between the simulated nanostructures and the SEM images taken on the respective experimentally produced nanofoam. In figure 2(d), a nanostructure simulated with $N_P = 1500$ (i.e. $\rho_f \simeq 9$ mg cm^{-3} for carbon nanoparticles) is shown in comparison to the SEM of a carbon nanofoam with average density of approximately 8 mg cm^{-3} presented in figure 2(e). The web-like structure typical of nanofoams in this range of density is visible in the simulated nanostructure, with void fractions having dimensions comparable to the experimental ones. In figures 2(f) and (g), the same comparison is made for a foam simulated with $N_P = 290$ (i.e. $\rho_f \simeq 28$ mg cm^{-3} for carbon nanoparticles) and a tree-like carbon nanofoam with an average density of 26 mg cm^{-3}. Even in this case, the mean pore dimension is comparable between the simulated and the experimental case. Correctly simulating these nanostructures can be fundamental in the understanding of experimental results on laser interaction with nanofoams and serves as input for particle-in-cell (PIC) codes [17, 58, 60–63].

2.3. Production of metallic foils for DLTs

Targets typically employed for TNSA, including DLTs, are usually based on metallic foils of micrometric thickness produced by mechanical processing of bulk materials (e.g. rolling). As a consequence, foils are characterised by the presence of defects such as ripples and pinholes, and by a high uncertainty on the thickness, which can show deviations of up to 30% within the same foil and between different foils. This is of major concern for shot-to-shot reproducibility [64]. Additionally, commercial foils are, generally, available in a limited range of thicknesses, not necessarily tailored to specific laser parameters. Consequently, the laser target coupling might not be optimised. Magnetron sputtering (MS) is a physical vapour deposition technique, particularly renowned for the production of near-bulk density metallic films, with tunable thickness (from few nm up to several μm) and composition, and great uniformity over large areas (several cm^{-2}). In this context, we have developed a procedure based on MS for the production of free-standing metallic foils, as outlined in figure 3(a). A solution of water and soap is spin-coated on a substrate (glass or silicon), forming a thin soap layer after water evaporation. MS deposition of the metallic film is performed on this nanometric sacrificial layer, which is then dissolved in water. At this point, the metallic film is detached from the substrate and floats on the water surface, enabling its fishing on the holder to be employed as a bare solid target [62]. Figure 3(b) shows the SEM image of a 50 nm-thick Al free-standing foil on a hole of the target holder, while figure 3(c) displays different thicknesses ranging from 50 nm up to 2 μm. A carbon nanofoam can be deposited via PLD on the free-standing foil to produce a DLT. Owing to their greater uniformity, sputtered foils allow one to obtain more reproducible results when compared to commercially available foils of the same thickness. This is highlighted in figures 3(d) and (e) which, for the first time, shows a comparison between proton spectra obtained with commercial 2 μm-Al foils and with sputtered 2 μm-Al foils, respectively, using the L3-HAPLS laser in the ELIMAIA beamline [65, 66] at ELI Beamlines (27 fs pulse-duration FWHM, 10 J pulse energy on target, elliptical focal spot with 1.5 μm×1.8 μm FWHM, s-polarisation, 15° incidence on target, 2×10^{21} W cm^{-2} peak intensity). As highlighted in figures 3(f) and (g), sputtered foils lead to more consistent results both in terms of the number of accelerated protons and their cut-off energy. This reproducibility is also important for achieving consistent results when DLTs are considered, since, also in this case, the solid layer thickness can affect the electron heating [62].

3. High-intensity laser-nanofoam interaction

Nano- and micro-structured near-critical density materials are widely employed in LPI across many different fields (e.g. ablators for inertial fusion confinement [21, 32], enhancement of laser-driven radiation sources [11, 31, 67]). The peculiar regime of interaction enabled by their density and morphology motivates the study of configurations employing these materials. When the focus is on nanofoams, their multi-scale morphology heavily influences the interaction regime. The interaction can be, in fact, characterised by processes which are either mediated by the nanometric scale of the particles composing the foam-e.g. the expansion or Coulomb explosion (CE) of the nanoparticles [60] and sub-wavelength scattering of the laser radiation [68]-or by the micrometric scale of the foam in terms of thickness and void volumes-e.g. deeper propagation of the laser inside the foam, shock formation [32], electron heating, activation of resonant processes such as direct-laser acceleration (DLA) [9, 10, 12] and relativistic self-focusing [13, 69]. Besides spatial scales, the time scales set by the laser pulse duration, i.e. picosecond/sub-picosecond or nanosecond, also determine which processes characterise the laser-nanofoam interaction. Indeed, the relativistic regime ($I > 10^{18}$ W cm^{-2} or $a_0 = eE_0/(m_e\omega c) > 1$), characterised by non-linear phenomena like relativistic self-induced transparency [70] and self-focusing, is usually achieved with short laser durations. In general, the short interaction timescale-when compared

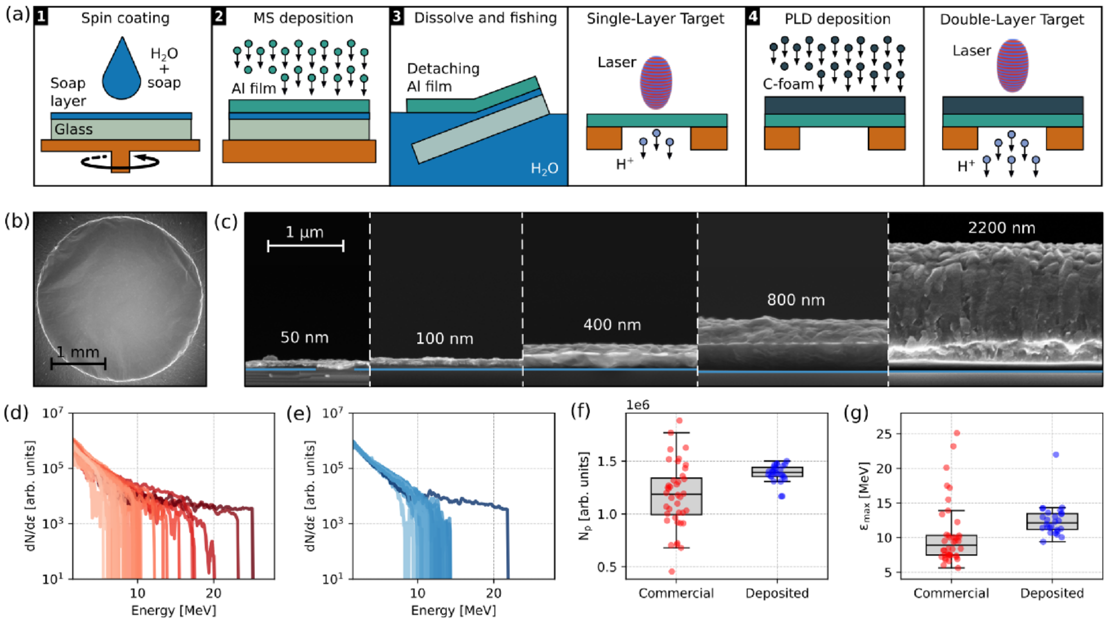

Figure 3. Solid foil and nanofoam-based DLT production. In (a), the step-by-step procedure for fully-optimised DLT production. In (b), a 50 nm-thick substrate lying over the circular aperture of a target holder. In (c), the SEM cross section images of 5 deposited substrates. Thicknesses are reported above each film. The 1 μm scale refers to all substrates. The blue horizontal line identifies the underside of the substrates. In (d), the proton spectra of 2 μm-thick Al commercial foils. In (e), the proton spectra of the 2 μm-thick Al sputtered foils. In (f), the comparison between the number of accelerated protons from commercial and sputtered Al targets, with the corresponding interquartile range, median, and whiskers. In (g), the comparison between the protons maximum energies obtained with commercial and deposited Al targets, with the corresponding interquartile range, median, and whiskers.

to the collisional time-and the high laser intensity make non-collisional and resonance mechanisms the primary source of laser energy absorption by the plasma particles in the sub-picosecond regime. Instead, in the nanosecond regime, collisional heating and plasma expansion dominate the interaction. In both temporal regimes, the presence of voids and the scattering of the laser field across the multiple nanoparticles allow the laser to propagate deeper than the typical skin depth of homogeneous layers with comparable density. This enables an increased volumetric heating. Moreover, the laser-nanofoam interaction is mediated by the homogenisation of the nanofoam itself, with strong effects on the absorbed laser fraction and plasma dynamics [32, 71]. The following two sections will be devoted to a deeper discussion of the two temporal regimes of laser interaction with nanofoams, with a review of already published results integrated with new simulations results on laser-nanofoam interaction at short timescales in the ultra-high-intensity regime.

3.1. Picosecond and sub-picoseconds lasers

These laser durations are particularly interesting because they allow for reaching ultra-high laser intensity and, thus, the relativistic regime. We will focus on this regime in the following, having in mind that non-relativistic ps/fs-laser interacting with nanofoam is a topic of equal importance from the point of view of many applications, including the understanding of the physics of fs-PLD. However, theoretically tackling it is very difficult because of the intertwining among out-of-equilibrium dynamics, collisional effects, and atomic phenomena.

Because of the relevance of non-linear, possibly relativistic, out-of-equilibrium, and kinetic effects, the ps/fs-laser regime is usually studied with PIC simulations [72–75]. PIC simulations can approximately solve the relativistic Vlasov-Maxwell system, usually neglecting collisions. Since the simulation timestep is typically set by the laser wavelength, and the spatial resolution is determined by the plasma Debye length or skin depth to capture the relevant physics, PIC simulations for laser-nanofoam interactions can describe sub-picosecond micrometric and nanometric scales. However, using PIC simulations when dense plasmas are involved and collisional corrections are required is challenging. In figure 4, a snapshot of an LPI simulation performed with the PIC code Smilei [73] is represented. The laser pulse has a duration of 25 fs, a waist of 3 μm, and $a_0 = 20$, while the carbon nanofoam has a density profile obtained with the code described in section 2.2 with an average density $\rho_f = n_c$. The nanofoam is initially fully

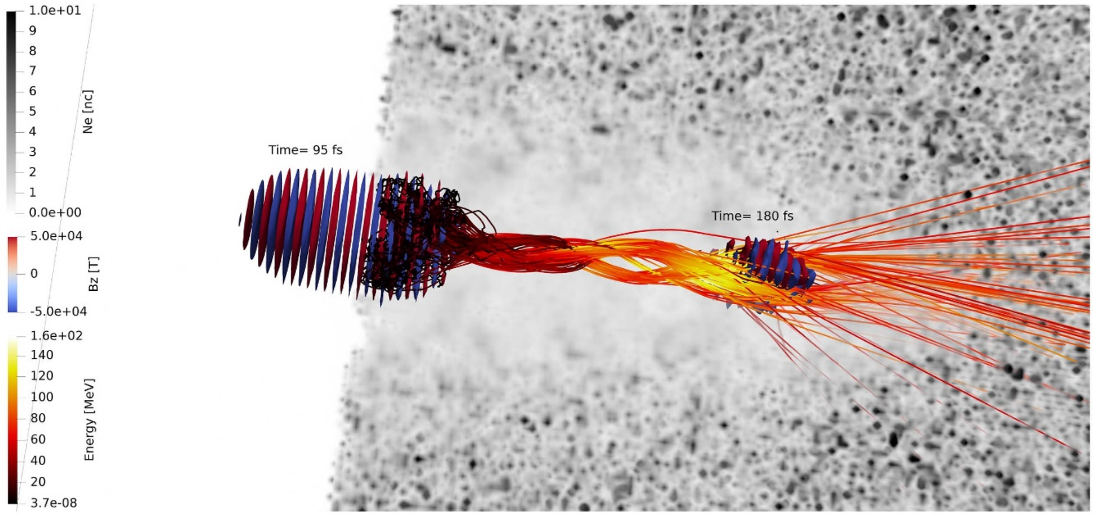

Figure 4. Snapshot of a Smilei PIC simulation of laser-nanofoam interaction. In the grey colour scale, the electron density of the carbon nanofoam with average density $\rho_f = n_c$. In red and blue scale, the contour of the component B_z of the laser pulse (25 fs-duration, $a_0 = 20$) at two times (beginning of the interaction with the nanofoam and before strong absorption starts). In the yellow-red colour scale, the trajectories of some of the most energetic electrons ($\varepsilon_e > 130$ MeV) accelerated by the laser pulse through the DLA process (their colour scales as their energy).

ionised, and no collisions or ionisation processes are included, as collisions have reduced impact in low-density targets and are relevant only at longer timescales, while the nanofoam ionisation at such intensities rapidly occurs due to the interaction of the target with the leading edge of the pulse. The method for integrating the simulated nanostructure in PIC simulations and further simulation parameters are detailed in the supplementary materials [76]. One can observe the nanofoam electron density in grey scale, the femtosecond laser B_z field contour in red and blue, and the trajectories of the most energetic electrons ($\varepsilon_e > 130$ MeV) coloured according to their energy.

When a relativistically intense sub-ps-laser interacts with a nanofoam, like in figure 4, its front tail rapidly ionises and expels electrons from its nanoparticles owing to the strong ponderomotive force exerted by the laser on the electrons. The homogenisation process of the foam is initiated and followed by the CE of the foam ions. Thanks, initially, to the micrometric voids of the foam structure and, subsequently, to the relativistic self-induced transparency, the focal region of the laser pulse can penetrate through the nanofoam while its front is progressively absorbed and steepened. In figure 4, the foam homogenisation in the channel created by the penetrating laser is visible. While traversing the foam, the laser heats a large fraction of the electrons roughly following the ponderomotive scaling [i.e. $\bar{\varepsilon}_e = (\sqrt{1 + a_0^2/2} - 1) m_e c^2$ for a linearly polarised pulse]. At the same time, a smaller fraction of electrons can match the conditions for super-ponderomotive heating and for starting processes characterised by coherent acceleration, like DLA. The activation of DLA is typical when the nanofoam average density approaches the value of n_c, and when the laser a_0 progressively increases.

DLA is characterised by the direct transfer of energy from laser to electrons [12]. In nanofoams, while the laser bores a channel in the homogenised electron density, some electrons are injected into this channel from its opening. An electric current develops in the channel and generates a quasi-static magnetic field, which further pinches the electrons in the channel and induces their oscillatory trajectories. When the frequency of these electron oscillations approaches the laser frequency seen by the electrons, the electrons can resonantly gain energy and increase their longitudinal momentum. All these features of the DLA process are recognisable in the wiggling trajectories of electrons gaining energy through DLA in figure 4. The processes of electron heating and DLA do not continue indefinitely since the laser pulse is progressively shaped and absorbed. Because of density depletion and relativistic effects due to the accelerated electrons [69, 77], the pulse is guided and focused inside the plasma until it reaches a peak in a_0. After that, defocus, absorption, and breaking in filaments prevail. The self-focusing of the laser pulse is particularly appreciable in figure 4.

The mentioned processes of nanoparticle homogenisation, ponderomotive heating, self-focusing, and coherent acceleration can all take place during ps and sub-ps laser interaction with nanofoam. However, the predominance of one aspect or the other essentially depends on the average density of the nanofoam and the laser a_0. At $a_0 \sim 1$, nanoparticle ionisation and homogenisation strongly affect the interaction. Fully ionisation is achieved only in a few localised spots. The nanofoam micrometric structures survive partly the laser passage and break the laser pulse front. Coherent acceleration is practically impossible, but electron heating creates a cloud of expanding energetic electrons. We anticipate that these aspects are relevant in laser interaction with the nanofoam of DLTs at low laser intensities as discussed in section 4.1 and shown in figure 7, where, in particular, the only partial ionisation of the material is appreciable. At $a_0 > 1$, we can consider homogenisation rapid and effective, especially for electrons: an almost homogeneous fully-ionised plasma is rapidly created by the front of the laser pulse. The results of PIC simulations with and without density nanostructures are qualitatively similar. According to the nanofoam density, different situations are encountered. Either self-focusing followed by laser absorption prevails, and DLA is marginal, or the laser propagates practically unchanged for tens of microns inside the foam, and DLA strongly contributes to increasing the energy of a bunch of electrons. In the first case, the analytical model by Pazzaglia *et al* [13] well describes the evolution of a_0 and the energy achieved by the heated electrons. In the second case, DLA modelling in nanofoams must be accounted for, and some results from general DLA literature can be used [78, 79]. As intensity further grows, $a_0 \gg 1$, DLA becomes prevailing at increasingly high nanofoam density.

The model by Pazzaglia *et al* [13] is essentially based on a thin-lens approximation for the homogenised foam action on the laser and a corrected ponderomotive scaling for electron heating. Here, we rewrite as a function of interaction time t the equations at the core of the model:

$$\frac{\mathrm{d}\varepsilon_l(t)}{\mathrm{d}t} = -\bar{\varepsilon}_\mathrm{e}(t)\frac{\mathrm{d}N_\mathrm{e}(t)}{\mathrm{d}t} \tag{3}$$

$$\varepsilon_l(t) = \varepsilon_{l0}\frac{a(t)^2 w(t)^2}{a_0 w_0} \tag{4}$$

$$\bar{\varepsilon}_\mathrm{e}(t) = C_\mathrm{nc} m_\mathrm{e} c^2 (\gamma(t) - 1) \tag{5}$$

$$\frac{\mathrm{d}N_\mathrm{e}(t)}{\mathrm{d}t} = \pi r_c^2 \rho_f c w(t)^2 \tag{6}$$

$$\gamma(t) = \sqrt{\frac{a(t)^2}{2} + 1} \tag{7}$$

$$w(t) = w_\mathrm{min}\sqrt{1 + \frac{[ct - l_f]^2}{x_r^2}} \tag{8}$$

$$w_\mathrm{min} = \frac{\lambda}{\pi}\sqrt{\frac{\gamma_0 n_\mathrm{c}}{\rho_f}},\ x_r = \frac{\pi w_\mathrm{min}}{\lambda} \tag{9}$$

$$l_f = \sqrt{x_r\left(\frac{\pi w_0^2}{\lambda} - x_r\right)} \tag{10}$$

where $\varepsilon_l(t)$ is the laser energy, which is depleted by laser energy absorption by foam electrons (absorption by ions is neglected). $\bar{\varepsilon}_\mathrm{e}(t)$ is the average energy of foam electrons, which follows a corrected ponderomotive scaling for the average time-dependent Lorentz factor $\gamma(t)$ dependent on the peak normalised vector potential $a(t)$. C_nc is a fitting parameter to consider a super-ponderomotive effect. $\mathrm{d}N_\mathrm{e}(t)/\mathrm{d}t$ is the number of electrons heated to this average energy per unit time. It is evaluated as the number of electrons in a cylindrical volume crossed by the laser in $\mathrm{d}t$ defined by the laser focal region. r_c is a fitting parameter to adjust the radius of this cylinder w.r.t. the laser waist $w(t)$, which is the time-dependent laser waist, evolving according to a thin-lens model for self-focusing in the foam. λ is the laser wavelength. The subscript zero identifies values of quantities at $t = 0$. w_min stands for the minimum waist achieved by the laser in the focusing process, and x_r and l_f are the corresponding Raleigh and focusing lengths. In [13], values for the fitting parameters are provided after comparison with PIC simulations performed for certain laser and foam parameters.

When foam densities are low and laser intensity increases, the model starts to fail because it neglects the DLA contribution, only partially considered through the super-ponderomotive coefficient. It is worth mentioning that a simplified version of this model, assuming $a(t) = a_0$ and $w(t) = w_0$ and without any fitting parameter, already works well in capturing the trends of laser energy conversion into electrons. Figure 5 shows this simplified model compared to electromagnetic (a) and electron (b) energy evolution in Smilei PIC simulations of a laser pulse of 25 fs and $w_0 = 3\,\mu$m interacting with a 60 μm foam with $\rho_f = n_\mathrm{c}$, like the one represented in figure 4. Simulations consider homogeneous morphology for the carbon nanofoam except for the cases in dotted lines, which consider a nanostructured morphology. In one simulation at the maximum a_0, both nanostructured morphology and radiation reaction effects, i.e. synchrotron-like photon emission, are included to get a more realistic picture. All input parameters

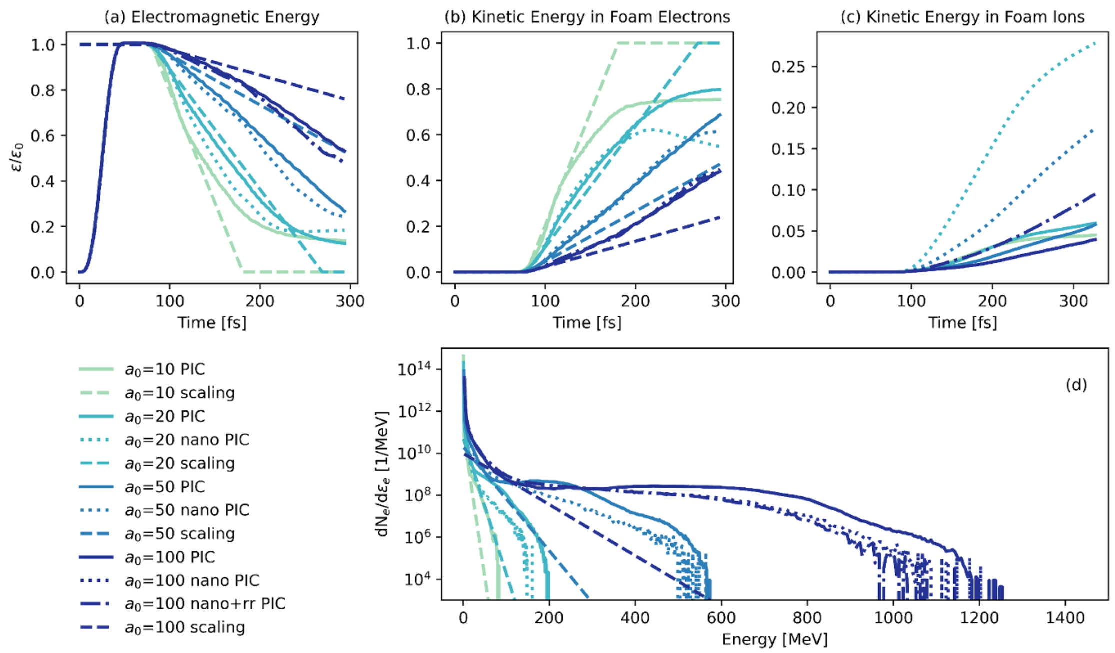

Figure 5. Evolution of electromagnetic energy (a), kinetic electron (b), and ion (c) energy during femtosecond laser interaction for different a_0 with nanofoam of mean density $1\,n_c$. In (d), the electron spectra at maximum energy. In solid lines, the results from Smilei PIC simulations. In dotted lines, PIC simulations including nanostructured morphology (nano). In dashed and dotted lines, a PIC simulation with nanostructured morphology and radiation reaction effects (rr). In dashed lines, the trends from the simple ponderomotive scaling reported in the text.

for these simulations are reported in the supplementary materials [76]. The increasing DLA contribution when increasing laser a_0 from 10 to 100 is what mainly causes deviation from the predicted laser depletion (electrons absorb more energy than expected because of this coherent process) and the deviation from a pure exponential behaviour $[\mathrm{d}N_\mathrm{e}/\mathrm{d}\varepsilon_\mathrm{e} = N_\mathrm{e}/\bar{\varepsilon}_\mathrm{e}\exp(-\varepsilon_\mathrm{e}/\bar{\varepsilon}_\mathrm{e})]$ for the spectra of accelerated electrons (panel (d) in figure 5). Indeed, the simplified scaling of the last panel fails to catch the high-energy tail distribution while it gets closer to the simulated spectra for intermediate energies around tens of MeV where it correctly gets the number of accelerated electrons. The simulation discrepancy with this scaling proves that physics causing super-ponderomotive heating of electrons must be accounted to perfectly match the trend of the spectra. The main effect of nanostructured morphology is the increase in the energy delivered to foam ions, which has a mild but visible effect on the laser and electron energy evolution, and a lowering of the high-energy component of the spectra, due to a slight reduction of coherency in acceleration. Since electrons accelerated through DLA can reach energies of hundreds of MeV or even GeV (see figure 5(d)), radiation reaction effects start to become important at $a_0 = 100$ and the high-energy tail of the electron spectrum is partially emptied.

3.2. Nanosecond lasers: studies and perspectives

At the nanosecond scales, nanofoam expansion and collisional, volumetric heating are the relevant processes. However, the kinetics of the nanofoam homogenisation occurring at shorter timescales has an impact on the nanosecond phenomena, modifying the laser absorption and, thus, the overall expansion. Indeed, the short and long timescale regimes are usually mixed and interconnected. Not only do the early steps (picosecond regime) of ns-laser-nanofoam interaction decide on how the interaction itself evolves, but also the fs-laser-nanofoam interaction is usually anticipated by the effect of nanosecond prepulses that induce foam pre-expansion. Due to this interplay between kinetic and long timescale phenomena, the interaction of ns-laser pulses with nanostructured materials-and with porous material in general-poses several challenges for its theoretical description [80].

From the numerical modelling side, the ns-laser interaction with targets is usually simulated through radiative hydrodynamics (RH) codes [81–84]. RH codes approximately simulate the plasmas under several limiting assumptions: quasi-neutrality of the plasma, local thermodynamic equilibrium, optically thick material, and ray-tracing methods for laser transport. These assumptions allow one to simplify the modelling, decreasing the computational cost associated with the simulations: the time-step is not related to the laser wavelength, and the plasma is considered as an expanding Eulerian fluid, often considering three temperatures to separately describe electrons, ions, and radiative emission. In this limit, the separation of charge is neglected, together with non-equilibrium effects induced by non-linear interaction between the laser and the plasma.

All these simplifications limit the application of fluid codes in the description of laser-nanofoam interaction, where the homogenisation process of the sub-wavelength nanoparticles cannot meet the conditions for simulation reliability. In this context, the use of fully electromagnetic kinetic codes, as already done for the fs-lasers, could guarantee a more reliable description. However, the limitations on the time-step given by the laser wavelength and the computational effort needed to resolve the complete phase-space make this approach unfeasible for current computing capabilities. A feasible-even though more approximate-approach is based on the integration of simplified homogenisation models into fluid codes, to generate a hybrid simulation environment. The simplified model treats the homogenisation of the foam on a subgrid, while the rest of the plasma is considered as a fluid. This approach has already been tested on microstructured foams, allowing for the description of the increased laser absorption, the different laser reflection, and the homogenisation process of the entire foam [20, 21, 85]. Some work was also made to increase the simplified model reliability, including kinetic effects [86], and comparing the model results to collisional PIC simulations [68].

A first study of this latter kind was also conducted on the numerical simulation of ns-laser interaction with nanofoams. The effects of the nanofoam structure were integrated by Maffini *et al* [32] in the 1D MULTI-FM [21] code, considering the nanofoam mean pore dimension and the average size of the nanofoam solid elements-i.e. the nanoparticle clusters encountered by the laser during its propagation-as significant parameters for the description of the process. The mean pore dimension and the solid element size were related to the foam density via the fractal scaling in equation (2), since they are associated with the average number of nanoparticles in a cluster N_P. For PLD-produced nanofoams, the proportionality factor was estimated by using the one given by Maffini *et al* [39]. This study highlighted a strong dependence of the shock propagation velocities on the nanostructure morphology. In particular, the presence of a nanostructure decreases the shock propagation velocity with respect to homogeneous materials, and a larger pore dimension leads to further reduction of the shock velocity. This investigation confirmed the importance of accurately simulating the nanostructure effects. These simulations have also been exploited to design an experimental campaign at the ABC laser facility (ENEA Research Center Frascati, Italy), aiming at investigating the potentialities of C nanofoams as ablation layers in ICF. An article regarding these experimental results is currently in preparation. Ongoing studies are devoted to increasing the modelling accuracy by including kinetic and electrostatic effects in the nanoparticle homogenisation, laser scattering by the foam nanoparticles, and multi-dimensional effects. Preliminary results show a non-negligible effect of the laser-induced charge separation, in sub-wavelength nanoparticles whose dimension is smaller than the laser skin depth, as for PLD-produced nanofoams. In fact, this characteristic enables non-collisional absorption mechanisms even at modest laser intensities.

4. Nanofoam-based DLTs for enhanced laser-based particle and radiation sources

The peculiarities of the high-intensity sub-ps laser interaction with low-density near-critical nanofoams have motivated the application of these materials for laser-based radiation source optimisation [11, 30, 31, 64, 87]. In fact, laser-based particle acceleration and generation mechanisms are mostly driven by hot electrons that are efficiently produced in laser interaction with near-critical nanofoams-with the processes described in section 3.1.

Among the others, the DLT configuration is one of the most studied for laser-based radiation sources [11, 30, 67]. The DLT, in general, is composed of a near-critical layer on top of a solid density layer: the near-critical layer plays the role of a driver for efficient electron acceleration, while the solid layer is used to meet the conditions for both strong charge separation-which drives the acceleration of the target contaminant ions in the TNSA mechanism [18]-and laser pulse reflection-which can initiate head-on collisions in the strong-field quantum-electrodynamics (SF-QED) regime among high-energy particles and intense electromagnetic fields [14, 15].

In this context, nanofoams provide a unique and versatile tool for the production of the near-critical layer of DLTs. The high control of their properties (morphology, mean density, and thickness) achievable with the PLD technique makes nanofoams an advanced tool for the study and the optimisation of DLT configurations. In the next sections, the main applications of nanofoam-based DLTs will be shown, and the challenges and open issues for their use in laser-based radiation sources will be assessed. This assessment will include a critical review of already published theoretical and experimental results. Those results will be integrated with new studies opening new perspectives on fewer studied regimes (i.e. particle acceleration at relatively low laser intensities).

4.1. Enhanced laser-driven ion acceleration using nanofoams

The interaction of relativistically intense lasers with solid targets has been studied and deployed since the beginning of the 2000 s as an alternative approach for ion acceleration [19, 88–90]. Among all the possible mechanisms, the TNSA process has been thoroughly studied and has been regarded as one of the most accessible with current laser capabilities. The basic principle relies on a relatively simple process: a short and intense laser adiabatically heats up the electrons in an overdense target. The electrons, during their expansion, generate a strong charge separation on a micrometric scale. A strong electrostatic field is generated and accelerates the superficial and low-mass contaminant ions-particularly protons-present on the solid target. This mechanism enables the acceleration of bunches of protons in a short timescale (i.e. the picosecond timescale); depending on laser pulse intensity, duration, and energy, approximately 10^9–10^{12} protons per laser shot are accelerated up to 10 s of MeV with a quasi-exponential energy spectrum [19, 91, 92].

The scaling laws derived for the TNSA regime predict a strong dependence of the maximum and mean energy of the accelerated ions on the mean energy possessed by the hot electrons-which is improperly referred to as the temperature of the electrons (T_e), due to the typical Maxwellian-like shape of their energy spectrum in laser-solid interaction. There are two main simplified theoretical approaches to describe the TNSA process. The first, by Mora [91], in which the TNSA process is modelled as a two-fluid expansion into vacuum driven by charge separation. In this description, the TNSA-accelerated protons present an exponentially decreasing energy spectrum up to a cut-off value $\varepsilon_{\mathrm{p,max}}$. The energy spectrum is described by the following formula:

$$\frac{\mathrm{d}N_\mathrm{p}}{\mathrm{d}\varepsilon_\mathrm{p}} = \frac{n_{\mathrm{p},0} c_s t}{\sqrt{2T_\mathrm{e}\varepsilon_\mathrm{p}}} \exp\left(-\sqrt{\frac{2T_\mathrm{e}}{\varepsilon_\mathrm{p}}}\right) \text{ for } \varepsilon_\mathrm{p} < \varepsilon_{\mathrm{p,max}}\,, \tag{11}$$

where ε_p is the proton energy, $c_s = T_\mathrm{e}/m_\mathrm{p}$ is the ion acoustic velocity, $n_{\mathrm{p},0}$ is the proton initial number density, m_p is the proton mass, t is the time from the start of the acceleration, and T_e is the temperature of the laser-heated electrons. Here, the maximum energy is inferred from the motion of the ion expansion front along time and diverges as t goes to infinity. Another approach, by Passoni *et al* [92], aims to derive the maximum proton energy from a quasi-static approach following a plasma sheath formation. The maximum proton energy is inferred in this case by the electrostatic potential generated by the plasma sheath at the surface of the target due to the hot electrons, and, thus, a finite value is achieved. The maximum energy scaling under these hypotheses is:

$$\varepsilon_{\mathrm{p,max}} = \varphi_0 T_\mathrm{e}\,, \tag{12}$$

where φ_0 is the normalised electrostatic potential at the target-vacuum interface, and T_e is the hot electron temperature. The potential depends on the physics of the laser interaction with the solid target and is related to the energy of the bound electrons in the target. Its value is related to the laser pulse energy through scaling laws fitted to the experimental data. The proportionality between the maximum energy and the temperature is guaranteed by the derivation of the scaling, which follows the electromagnetic potential normalisation with respect to the electron temperature. The scaling law can be generalised also to non-Maxwellian electron energy distributions, with non-negligible effects in the maximum proton energy [93]. However, such approach does not lead to simple analytical formulae. In such cases, the use of the second moment of the electron distribution function, i.e. the mean electron energy, in place of the temperature can still guarantee a satisfactory approximation of the proton energy, keeping the intrinsic simplicity of the scaling law.

In both cases, one can observe the strong dependence of the proton energy on the mean electron energy. However, in the interaction of a laser with an overdense target, the mean electron energy is limited by the ponderomotive scaling [94]-in the simplest picture, which neglects more complex mechanisms [95]. While lowering the target thickness can be considered beneficial in increasing the mean electron energy, due to the enhanced recirculation effects [96], another approach consists in placing a near-critical layer on the target surface facing the impinging laser pulse [11]. Such a near-critical layer can be a PLD-deposited nanofoam, exploiting the nanofoam-based DLT scheme [87]. The DLT enables the resonant and non-linear effects-i.e. DLA-described in section 3.1. The laser absorption by the target electrons is, thus, enhanced, and the mean electron energy is increased. These effects on the mean electron energy benefit the proton acceleration, allowing for a more efficient acceleration regime; following the work by Pazzaglia *et al*[13], the quasi-static model [92] can be employed to estimate the proton maximum energy increase due to the near-critical layer. The hot-electron mean

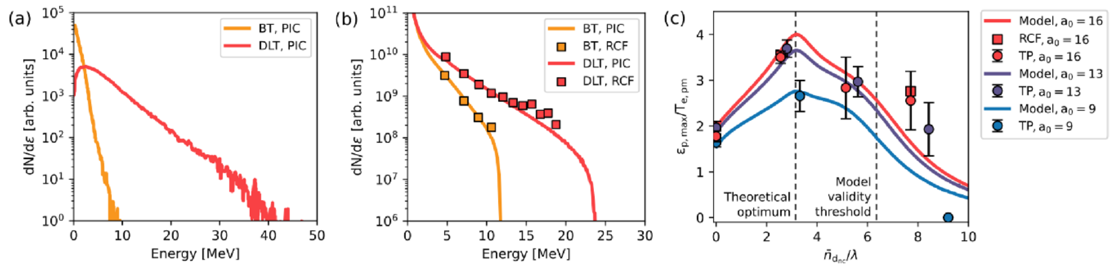

Figure 6. Modelling and experimental results of TNSA driven by DLTs. In (a), the electron energy spectrum from PIC simulations of a laser interacting with an aluminium foil (BT, in yellow) and a nanofoam-based DLT (in red) is shown. In (b), the respective TNSA proton energy spectra are shown in comparison with experimental data from RCFs, shown as square markers. In (c), the results of the theoretical model by Pazzaglia *et al* [13] applied to different experimental conditions are compared with experimental data from RCFs (square markers) and TP (dots). Here, $\varepsilon_{\mathrm{p,max}}$ is the maximum proton energy, $T_{\mathrm{e,pm}}$ is the electron mean energy estimated via ponderomotive scaling, $\overline{n} = n_{\mathrm{e}}/\gamma n_{\mathrm{c}}$, with n_{e} the electron density of the foam layer, γ the relativistic factor computed with equation (7) for $t = 0$, and d_{nc} is the foam thickness.

energy $\overline{T}_{\mathrm{e}}$ is estimated by:

$$\overline{T}_{\mathrm{e}} = \frac{N_{\mathrm{e,foam}} T_{\mathrm{e,foam}} + N_{\mathrm{e,foil}} T_{\mathrm{e,foil}}}{N_{\mathrm{e,foam}} + N_{\mathrm{e,foil}}} \,, \tag{13}$$

where $N_{\mathrm{e,foam}}$ is the number of hot electrons accelerated by the laser in the near-critical layer-evaluated as the time integral of equation (6)-, $T_{\mathrm{e,foam}}$ is the mean energy of the electrons accelerated by the laser in the near-critical layer-i.e. $\overline{\varepsilon}_{\mathrm{e}}$ computed with equation (5)-, $N_{\mathrm{e,foil}}$ is the number of hot electrons accelerated by the laser in the solid foil, and $T_{\mathrm{e,foil}}$ is the mean energy of the electrons accelerated by the laser in the solid foil, heated up by ponderomotive scaling by the laser pulse at the foam/solid interface. Therefore, $\overline{T}_{\mathrm{e}}$ represents the average energy between the electrons accelerated in the near-critical layer and those heated up in the overdense layer. This approximation allows one to obtain a satisfactory estimation of the proton maximum energy, which can be maximised for optimal values of the near-critical layer density and thickness. Under these hypotheses, the optimal foam thickness coincides with the laser self-focusing length in the near-critical layer expressed by equation (10). Indeed, for a foam length equal to the self-focusing length, electron heating is effective in the foam and the laser pulse has still enough energy to start heating the solid substrate.

Experimental and simulation results confirm these theoretical observations. Here, we report PIC simulations, presented by Maffini *et al* [61] and performed at relevant experimental conditions-i.e. to reproduce the experimental data from Prencipe *et al* [31]. They were performed with the PIC code PICCANTE [97] and considered the interaction of a 150-TW laser ($a_0 = 16$, 2.8 μm focal-spot FWHM, $\lambda = 0.8\,\mu$m, p-polarisation, 30 fs pulse-duration FWHM, Gaussian envelope) with a 1.5 μm-thick aluminium foil and with an optimised nanostructured DLT-composed of a 4 μm-thick foam layer simulated with the DLCCA code presented in section 2.2 with a mean density of 3 n_{c} on top of a 1.5 μm-thick aluminium foil. In figure 6(a), the electron spectra from the two PIC simulations considering the aluminium foil [bare target (BT)] and the optimised DLT are shown. As expected, the mean electron energy from the DLT simulation exceeds the mean electron energy from the BT thanks to the processes described in section 3.1. Following equation (12), the increase in the mean electron energy results in an increase in the maximum proton energy. In figure 6(b), the proton spectra from the BT and DLT simulations are reported, confirming the theoretical trend. The proton spectra from the simulations are also compared with the experimental radiochromic film (RCF) data from Prencipe *et al* [31]-represented as square markers in the plot. The agreement between the experimental proton spectra and those of simulations also confirms experimentally the role of the nanofoam in increasing the laser energy absorption by the electrons and the proton maximum energy. In figure 6(c), the comparison between the experimental data from Prencipe *et al* [31] and the theoretical model by Pazzaglia *et al* for the TNSA from DLTs is presented. The experimental data are presented at varying nanofoam thickness and laser pulse energy. By inspecting the data and comparing them with the theoretical results, one can observe a good agreement in the model range of validity. The model can reproduce the optimal foam thickness retrieved in the experimental data, confirming the relevance of the self-focusing effect in the TNSA optimisation for not-too-intense and not-strongly-focused laser pulses.

When the laser intensity is such that the nanofoam is not completely ionised-i.e. when $a_0 \approx 1$-, the homogenisation process of the electron density in the laser channel happens at longer timescales than those of the interaction, as anticipated in section 3.1. While the TNSA could benefit from an increased

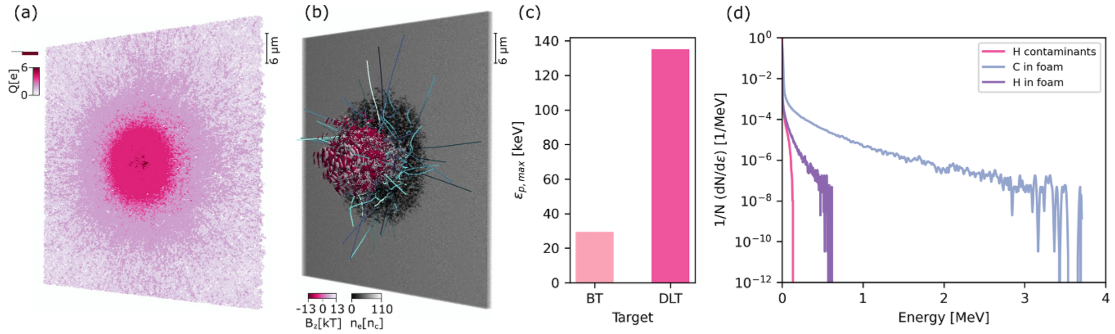

Figure 7. Laser interaction with nanofoam-based DLT at $a_0 = 1.4$. In (a), the ionisation state of the foam carbon ions at the end of the simulation is presented. In (b), the snapshot of a simulation of a laser interacting with a nanostructured ionising DLT is shown. The snapshot represents the electron density 100 fs after the start of the simulation, together with a contour of the z component of the laser magnetic field (pink colour map) and the trajectories of some test electrons (in blue). In (c), the maximum proton energy from TNSA is shown for a solid foil (BT) in light pink and the DLT case in dark pink. In (d), the normalised energy spectra from the DLT simulation of contaminant ions (in dark pink) and carbon ions (in light blue) are shown. In purple, the carbon ion spectrum rescaled for a particle having the charge of a proton is presented.

mean electron energy even at this relatively low intensity, the nanostructure could enable more efficient ion acceleration processes, such as CE. To study these effects, we performed two 3D SMILEI [73] simulations, considering again the interaction of a laser with both a BT and a DLT. The simulated laser pulse aims at reproducing an experimental setup based on a table-top sub-TW laser of 10 fs duration, 2.5 μm waist and $a_0 = 1.4$ [98]. The pulse interacts with a DLT composed of a carbon nanofoam simulated according to section 2.2 with an average density of 0.95 n_c and thickness of 3.07 μm on top of a 1 μm-thick aluminium substrate. Detailed input parameters for these simulations are given in the supplementary materials [76]. Collisions and radiation reaction effects were neglected in the simulation, to avoid the increased computational costs and numerical heating related to adding the MC processes within the PIC loop. While the latter are not expected to affect the dynamics of the system due to the relatively low intensity, collisions causing ionisation and energy absorption are expected to affect the process, by increasing the mean ionisation state and the absorbed energy fraction, respectively. However, due to the short timescale (∼10 fs) of the interaction, their effects are not expected to modify the observable trends. Moreover, the tunnelling ionisation of the carbon nanofoam is simulated. The barrier suppression ionisation is, instead, neglected since its effects should be negligible at $a_0 \simeq 1$. The nanofoam ionisation is simulated as a mono-atomic carbon gas at solid density, i.e. neglecting the solid-state electronic bands of the graphite that composes the foam nanoparticles. Thus, the ionisation state cannot be quantitatively estimated. Nevertheless, the simulations are expected to qualitatively reproduce the trends, giving an insight in the physical process.

In figure 7(a), the foam carbon ionisation state at the end of the simulation is presented. As already discussed in section 3.1, one can observe from the plot that the totally ionised carbon ion is only present in a few spots, located where the laser intensity is at its maximum. In figure 7(b), a snapshot of the plasma electron density of the DLT at 100 fs from the simulation start is shown. In the picture, the contour of the magnetic field along the z-direction and the trajectories of test electrons placed in the nanofoam are also shown. One can observe the ionisation front in the nanofoam due to the tunnel ionisation induced by the laser pulse. Moreover, the non-uniform shaping of the reflected laser suggests that light scattering with the foam nanoparticles affects the interaction, confirming that the homogenisation process is not completed during the interaction. In figure 7(c), the comparison in terms of maximum proton energy at the end of the simulation ($\varepsilon_{\mathrm{p,max}}$) between the TNSA driven by the BT and that of the DLT is shown. As expected, the increased laser energy absorption by the DLT electrons drives a more sustained accelerating field for the contaminants; the accelerated protons approach an energy approximately 5 times higher than that of the BT. Instead, in figure 7(d), the energy spectra of the TNSA accelerated ions (in pink) and of the nanofoam carbons (in light blue) are shown. In purple, the carbon energy spectrum rescaled by the maximum ion charge in the foam is presented-i.e. the charge of the maximum carbon charge state retrieved in the simulation. By inspecting the results, one can observe the CE to be more efficient than TNSA in accelerating the particles in this regime. The maximum electric field that a proton would feel in the same Coulomb potential as of the nanofoam carbons can be effectively estimated by dividing the maximum carbon energy by the maximum carbon charge. Under this hypothesis, the maximum energy a proton would reach due to the CE of the nanoparticles is approximately 6 times higher than that of TNSA. This suggests that the use of CH_2 nanofoams (presented in section 2.1.2) could enhance the laser energy conversion into proton energy. However, the isotropic emission of protons due to CE on nanospheres would increase the radiation divergence. While this could be a problem for applications of energetic protons that rely on the directionality of the radiation, the generation of such energetic protons inside the foam could be beneficial for the production of in-target nuclear reactions. In fact, this configuration could enable the production of α particles or neutrons directly in the target, even at modest laser intensity, by co-depositing CH_2 with proper converters and/or dopants.

4.2. Gamma and positron sources using nanofoams

The processes of electron heating and acceleration by a relativistic pulse interacting with a nanofoam (see section 3.1) are also drivers for secondary sources of high-energy photons (MeV range) and positrons. In this context, the processes relevant for generating secondary sources of photons are: the electron scattering in the Coulomb field of ions and atoms of the plasma, i.e. bremsstrahlung [99], the electron scattering in quasi-static magnetic or electric fields generated in the plasma, also called betatron emission [100, 101], and the electron multiple scattering with the low-energy laser photons in the intense laser electromagnetic field, i.e. non-linear inverse Compton scattering (NICS) [14, 102]. Instead, for the generation of positrons, the processes to consider are the multiple scattering of photons with the low-energy laser photons in intense electromagnetic fields, i.e. non-linear Breit–Wheeler pair production (NBW) [14, 102], and the photon scattering in the Coulomb field, i.e. Bethe–Heitler pair production (BH) [103].

NICS and NBW have a much higher probability of occurring in the head-on collision of electrons/photons with the laser, while they are almost suppressed in the case of particle co-propagation with the laser pulse. Bremsstrahlung and BH cross-sections both show a strong dependence on target atomic number and density. Consequently, when the laser pulse simply propagates in a nanofoam, high-energy photons can mainly come from the scattering of wiggling accelerated electrons in the quasi-static fields, i.e. betatron emission, while bremsstrahlung and NICS cannot give an appreciable contribution. However, as anticipated, when considering a DLT produced with a nanofoam, the presence of the solid substrate can activate these other processes. The substrate reflects the non-absorbed laser, creating the conditions for head-on laser-particle collisions necessary for NICS and NBW. Moreover, if it is thick enough, dense enough, and with a high atomic number, it creates the conditions for efficient particle-matter interactions, like bremsstrahlung and BH.

The nanofoam-based DLT scheme for high-energy photon generation has been analysed in depth in 2D and 3D numerical studies considering bremsstrahlung contribution in thin [104] and thick substrates [105] with $a_0 < 20$, NICS at higher intensities ($a_0 > 20$) [106], and compresence of bremsstrahlung and NICS in thin targets at $a_0 = 20$ [16]. Finally, NICS and NBW at high intensities ($a_0 \geq 40$) have been explored mimicking realistic experimental conditions [17]. These numerical works have confirmed the interest in exploiting nanofoam-based DLT for the production of gamma photons with broad exponential spectra up to hundreds of MeV using available laser facilities, both through bremsstrahlung and NICS. Moreover, NBW could be explored in future facilities (accessing $a_0 \sim 150$) with the same target scheme, which additionally allows for selecting and accelerating positrons thanks to the sheath fields generated at the back of the DLT [17].

4.3. Open issues towards nanofoam-enhanced laser-based radiation sources

As discussed in the previous sections, nanofoam-based DLTs enable a better laser-plasma coupling, allowing for an enhancement in particle acceleration and generation efficiency. However, the nanofoam structure in DLTs is extremely delicate, and any damage occurring in the low-density layer before the interaction with the laser pulse can lead to a significant loss in acceleration performances.

The target damage, even in the case of BTs, is influenced by several factors. Among these, the prepulse plays a significant role. The shock generated by the prepulse interaction with the target may result in a displacement of the target from the focal plane and in a deformation of its surface before the main pulse interaction. This effect leads to a reduction in the maximum proton energy and an increase in the beam divergence [107]. Moreover, the duration and intensity of the laser pedestal have a strong impact on the target properties-e.g. by modifying the thickness and density at the moment of the main pulse interaction with the target. The proton acceleration optimisation is, thus, achieved with a proper counterbalance between recirculation effects given by the thickness reduction and target integrity at the moment of the main pulse interaction. In this sense, the prepulse properties directly affect both the optimal target thickness and the maximum achievable beam energy, by posing a lower limit in the usable target thickness [108–110]. All these effects are present even in the case of nanofoam-based DLTs, where the nanofoam properties can be heavily modified by the prepulse (i.e. morphology, density, and thickness). The acceleration optimisation should, then, account for these modifications.

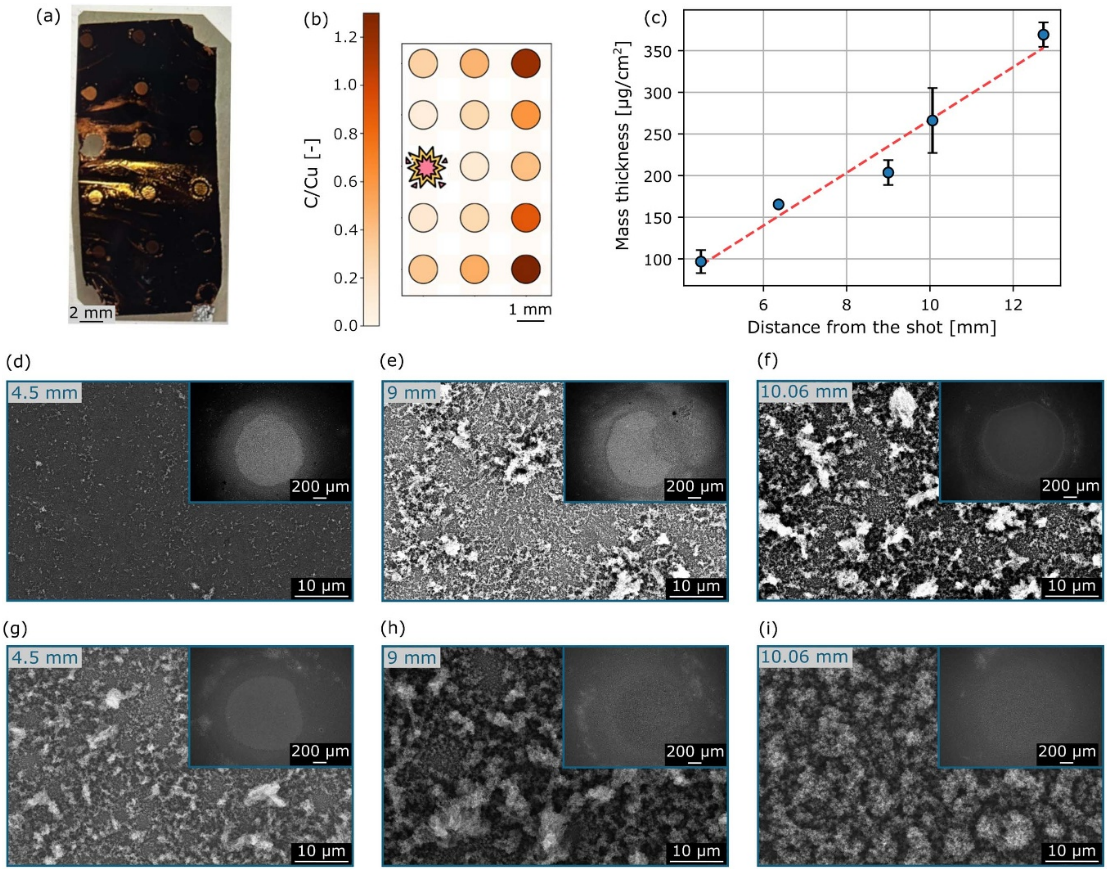

Figure 8. Damage induced on nanofoam-based DLTs by a single laser shot. In (a), a 20 mg cm^{-3}—20 μm nanofoam-based DLT after laser irradiation at ELI Beamlines. In (b), the C/Cu areal peak ratio at increasing distance from the shot from EDX analysis, considering the neighbouring holes in the target holder. In (c), the residual foam-mass-thickness radial evolution after irradiation. In (d), (e), and (f), the SEM images at various distances from the shot for a 20 mg cm^{-3} C-nanofoam-based DLT irradiated with 10 J laser pulses at ELI Beamlines. In (g), (h), and (i), the SEM images at various distances from the shot for a 20 mg cm^{-3} C-nanofoam-based DLT irradiated with 2.27 J laser pulses at ELI Beamlines.

Additionally, the damage can extend beyond the laser spot through several mechanisms. When a high-intensity pulse interacts with the target material, part of the latter is vaporised and generates high-energy debris. These, together with the propagation of shock and heat waves, and the interaction with any unfocused light, can damage the target even several millimetres away from the interaction point. As a result, the structural integrity of the material may be compromised, and the target cannot operate properly any more-i.e. the laser-target coupling is not optimised due to target modifications and foam removal [87]. This effect becomes critical in high-repetition-rate facilities. Here, the decrease in efficiency of the laser-plasma coupling may occur during subsequent shots because of foam removal due to previous ones, affecting the stability of the accelerated beam. Consequently, a deeper understanding of the mechanisms and properties underlying the target damage is required to develop effective mitigation strategies.

With this aim, we carried out several characterisations on DLTs used for two experimental campaigns at PW-class laser facilities, using the 1-PW L3-HAPLS laser driving the ELIMAIA beamline at ELI Beamlines [65, 66] and the 1-PW F2 laser at the Apollon facility [111, 112]. In these campaigns, optimised DLTs either for ion acceleration or for high-energy photon production were produced-at the ELI facility and at the Apollon facility, respectively. The targets properties were characterised both before and after-i.e. post-mortem-laser irradiation, and they were compared to assess the extent of the reported damage. The results of this characterisation are reported in the following for both experiments.

Figure 8(a) shows the results of a DLT tested during the campaign at ELI. The target consists in a 2 μm-thick copper foil coated with 20 μm-thick carbon nanofoam with a density of 20 mg cm^{-3}-i.e. a tree-like foam. The target was irradiated by a single shot with the same laser parameters as those presented in section 2.3. Similarly to other experiments [87], the foam is damaged in the neighbouring region of the shot, despite the absence of a direct irradiation. Figures 8(b) and (c) present the results of EDX analysis performed in correspondence of the target holder holes in the neighbourhood of the irradiation

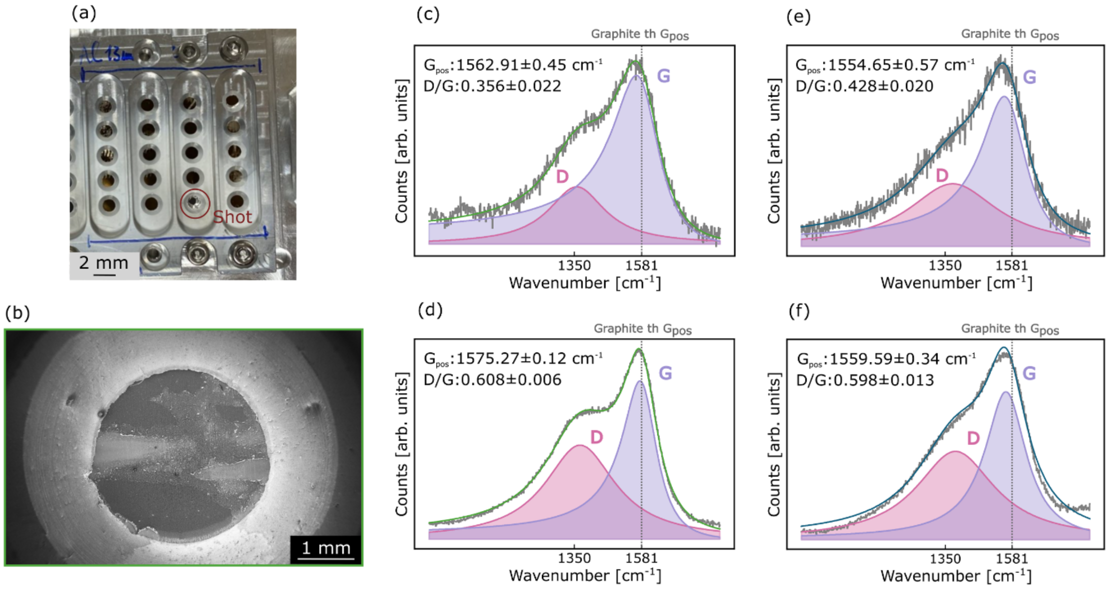

Figure 9. Comparison between targets irradiated at Apollon and ELI facilities. In (a), the Apollon target holder after irradiation. In (b), the SEM image of a damaged shot neighbour hole in the target holder. In (c) and (d), the Raman spectra of the damaged foam before and after irradiation at Apollon, respectively. In (e) and (f), the Raman spectra of the damaged foam before and after irradiation at ELI Beamlines, respectively.

point-i.e. on the damaged neighbours of the shot. We examined the areal density evolution using the procedure by Pazzaglia *et al* [47] based on EDX measurements. From this characterisation, one can note an increase in the foam areal density with increasing distance with respect to the irradiated point. This can be interpreted as a decreasing damage with increasing distance from irradiation, displayed, thus, with a radial trend. Moreover, the affected area shows a millimetre scale, orders of magnitude higher than the micrometre-scale laser spot, confirming the influence of the aforementioned processes in the target damaging.

In figures 8(d)–(i), SEM images of damaged neighbours of DLTs used at ELI Beamlines are shown at increasing distance from the interaction point and at different pulse energies-keeping temporal and spatial profiles constant. Figures 8(d)–(f) show results for 10 J irradiation and figures 8(g)–(i) show results for 2.27 J irradiation. By inspecting these SEM images, changes in the material morphology following irradiation are visible. By comparing these results with those of EDX, an increase in the amount of residual foam can be observed with increasing distance from the shot. Moreover, the surface morphology progressively approaches the pristine condition. This behaviour becomes even more evident for lower pulse energy; here, the morphology appears almost identical to that of the as-deposited material even for short distances from the irradiation point. Furthermore, in both cases, the nanofoam is uniformly removed by each neighbour and no localised damage is reported. This damage might, then, be related to a mechanical remotion of the nanofoam following the propagation of a shock wave, rather than damage due to impact with debris which would be more localised.

A different behaviour was observed for the targets irradiated at Apollon. In this case, we employed 13 μm-thick aluminium foils coated with 40 μm carbon nanofoams with a density of 10 mg cm^{-3}-i.e. web-like foams. In figure 9(a) the post-mortem condition of an irradiated target in the respective target holder is shown. Unlike the ELI targets, the post-mortem analysis of the samples reveals that the damage does not follow any clear trend with distance from the laser shot, and the non-irradiated holes in the neighbourhood of the laser shot exhibit different damage patterns. In figure 9(b), a SEM image of one of the neighbours of the shot is presented. The image highlights how the foam removal is not uniform across the target holder aperture. Rather, it is localised along thin streaks, suggesting that the damage is more likely related to laser interaction, than to mechanical behaviour. This interpretation is supported by the higher thickness of the aluminium foils compared to the thinner copper targets used at ELI. The latter, are more prone to 'vibrating membrane-like' effects, so, to a mechanical removal of the foam.

To further investigate the damage mechanism, Raman spectroscopy was performed on damaged areas before and after laser irradiation. By comparing the Raman spectra of the pristine and post-irradiated targets used at Apollon (figures 9(c) and (d), respectively) and ELI (figures 9(e) and (f), respectively), one observes a larger G-band shift towards the theoretical graphite-G-peak (found at 1581 cm^{-1}) with respect to the pristine target in those irradiated at Apollon. This shift, together with the increase in the intensity ratio of the D and G-bands, indicates a stronger local heating. This leads to a structural reorganisation of the carbon lattice and, thus, to an increase in the graphitic component in the nanofoam [113]. In contrast, the smaller shift observed for the ELI samples-in which the post-mortem condition is quite similar to the as deposited one-supports the hypothesis of a predominantly mechanical damage induced by shock propagation in the thinner targets. These results give important insight on how DLTs damage after irradiation showing a role of the substrate in defining the damage processes happening during the target irradiation. Moreover, they highlight the importance of the design of target holders in enabling the high-repetition-rate operation of more complex targets such as nanofoam-based DLTs.

5. DLT for enhanced secondary particle and radiation sources—applications

As discussed in the Introduction, the potential use of laser-driven radiation sources can span a wide range of applications. The versatility in tuning the type of radiation (e.g. electrons, ions, γ rays and positrons) and its energy by adjusting the properties of the laser pulse (e.g. intensity, pulse duration, energy, focal spot) and of the target (e.g. composition, thickness, surface conditioning) makes laser-driven sources appealing in many sectors of scientific investigation. Moreover, secondary radiation can also be generated by exploiting the interaction of the accelerated radiation with suitable converters-e.g. neutrons generated via (p, n) nuclear reactions, bremsstrahlung with high-Z materials. Unlike electrostatic accelerators, laser-based radiation sources do not require relatively long ramp-up and ramp-down times. Furthermore, since particle acceleration is confined to distances of a few tens of micrometres, the radiation protection issues are lower when compared to conventional accelerators.

Many application domains are currently under investigation for laser-driven sources [18, 58, 114]. Among them, one can find materials science, nuclear medicine, and imaging of large objects at customs or border control points. In all these contexts, nanofoam-based DLTs may play a crucial role. In fact, keeping laser parameters fixed, DLTs could enhance the system performance, thereby enabling applications that are not achievable with conventional targets based on solid foils. In addition, they could also mitigate the requirements on the laser system, paving the way for more compact and reliable solutions, which could potentially enable the design of transportable configurations.

In this section, we will focus on three relevant applications of laser-driven proton sources, performing novel comparisons of the yields possibly achievable from solid foils with those from nanofoam-based DLTs, keeping laser pulse parameters fixed: neutron generation, production of radioisotopes (i.e. C-11), and PIXE. The first two rely on a *pitcher-catcher* configuration, in which protons are directed onto a secondary material to induce suitable nuclear reactions. Instead, PIXE is studied in the full-field (FF) configuration to perform elemental mapping of inhomogeneous samples. Notably, 150 W-power laser systems with parameters (30 fs intensity FWMH, 2.8 μm focal spot FWHM, and normalised laser peak intensity $a_0 = 16$) consistent with those considered for this study are commercially available.

All three case studies are investigated through Geant4 [115] MC simulations, to compare, at fixed laser parameters, the performances of sources based on solid foils and DLTs. For each application, we employ the proton spectra obtained from the PIC simulations discussed in section 4. These spectra are reproduced in figure 10(a) and are in excellent agreement with experimental data. We assume a number of accelerated protons (N_p) per shot of 2.6×10^{10} above 2 MeV for the single-layer target, consistent with the experimental scaling reported by Mirani *et al* [116]. For DLTs, the number of protons is rescaled by a gain factor of 2.2, in line with experimental results by Prencipe *et al* [31]. Considering neutron generation and radioisotope production, we also investigate how the density and thickness of the near-critical layer affect the yield of the nuclear reactions involved, based on the model by Pazzaglia *et al* [13] described in section 3.1.

5.1. Neutron generation

Neutron generation from laser-driven sources has been the subject of extensive research in recent years [64, 117–119]. In one of the most studied configurations, protons are directed onto a converter material, where nuclear reactions occur, leading to neutron emission. Examples of such reactions include $^{9}\mathrm{Be}(p,n)^{9}\mathrm{B}$, $^{7}\mathrm{Li}(p,n)^{7}\mathrm{Be}$ and $^{63}\mathrm{Cu}(p,n)^{63}\mathrm{Zn}$. In this work, we focus on the $^{7}\mathrm{Li}(p,n)^{7}\mathrm{Be}$ reaction induced in a lithium fluoride converter; lithium fluoride is a chemically stable compound, and the isotope ($^{7}\mathrm{Li}$) involved in the nuclear reaction is found in nature with a high abundance of 92.5%. In addition, it shows a high cross-section at relatively low energies (see figure 10(a)).

To study this configuration, we perform two MC simulations in which a lithium fluoride disk (3 mm thickness, 4 cm diameter) is irradiated with protons whose energies were sampled from the aforementioned spectra. In both cases, 1.6×10^{8} primary protons are simulated, and the results are rescaled to

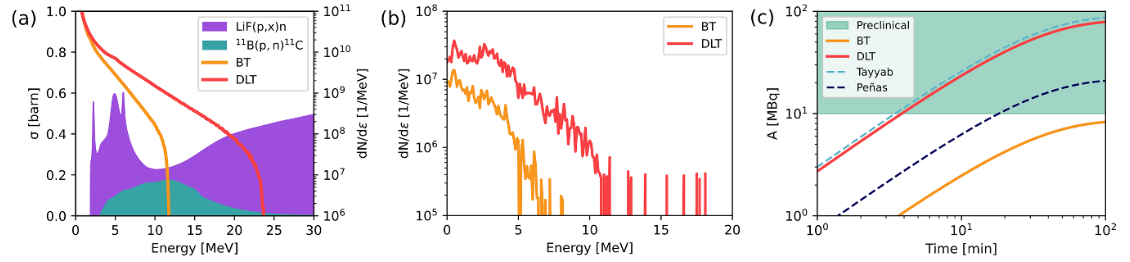

Figure 10. Laser-driven neutron and ^{11}C production with BTs and DLTs. In (a), the proton energy spectra from BT (yellow line) and DLT (red line) superimposed to the LiF total neutron production (filled purple) and $^{11}\mathrm{B}(p,n)^{11}\mathrm{C}$ (filled green) cross sections. In (b), the neutron energy spectra from BT (yellow line) and DLT (red line). In (c), the ^{11}C activity as a function of time from BT (yellow line), DLT (red line), Tayyab *et al* [121] (light blue) and Peñas *et al* [122] (dark blue). The green regions identifies activity values suitable for preclinical studies.

the effective number of protons per shot achievable with the two targets. To properly model the relevant nuclear reactions, we employ the `G4HadronPhysicsQGSP_BIC_AllHP` physics list, which makes use of cross-sections from the ENDF/B-VII.1 data libraries. We also include the `G4RadioactiveDecayPhysics` list, and the production cuts are set to 10 μm for all secondary particles. Electromagnetic processes are modelled using the `G4EmStandardPhysics_option4` module.

The neutron spectra emitted per shot from the rear face of the converter are shown in figure 10(b) for BTs and DLTs. Consistently with the proton spectra, the maximum energy of neutrons emitted with DLTs is about twice that observed with solid foils. The number of emitted neutrons per shot is 1.22×10^8 and 2.85×10^7, respectively for the two targets. Assuming a uniform angular distribution between the target normal and 70° [116], and a laser repetition rate (RR) of 10 Hz, we can estimate 5.48×10^7 and 2.34×10^8 n/sr/s for the BT and DLT configurations, respectively. These neutron yields are comparable to those obtained with state-of-the-art commercial fast neutron generators [120] used to perform neutron activation analysis (NAA) on materials with unknown bulk composition. It is worth noting that nanofoam-based DLTs would make the measurement four times faster compared to conventional targets, under identical laser conditions.

5.2. C-11 radioisotope production

The demand for radio-pharmaceuticals for medical applications-such as positron-emission tomography-is expected to increase in the coming years, and new solutions are needed to meet the rising demand [123]. In this context, the study of radioisotope production using laser-driven proton sources has become an area of growing interest [124–127], and strategies to optimise the process have been proposed to enhance the production yield [61, 128]. In a previous work [61], we investigated the use of laser-driven radiation sources based on DLTs for the production of ^{64}Cu, a radioisotope of particular relevance for theranostics. Here, we study the production of ^{11}C radioisotope through the nuclear reaction $^{11}\mathrm{B}(p,n)^{11}\mathrm{C}$. This isotope is characterised by its relatively short half-life $t_{1/2} = 20.39$ minutes. Thus, its on-site production is highly desirable both in hospitals and research centres-that routinely perform preclinical studies. For this reason, the exploration of its production with compact and cost-effective radiation sources, such as laser-driven proton sources, is of great interest.

As per the previous section, two simulations are carried out using as input the proton spectra from the BTs and the DLTs in section 4.1. Protons impinge on a volume of natural boron (i.e. containing 80.1% of ^{11}B) whose thickness can completely stop the highest-energy protons. A total number of 10^8 protons is simulated for both cases, and the results are rescaled to the actual number of protons per shot achievable with the two targets. The physical models implemented in the simulations are the same as those already mentioned in section 5.1. The cross-section for the $^{11}\mathrm{B}(p,n)^{11}\mathrm{C}$ reaction is reported in figure 10(a).

The yield (Y) of ^{11}C per incident proton is 1.01×10^{-4} and 2.73×10^{-4} for the BT and DLT, respectively. This difference in the yield is solely attributable to the higher proton energy achievable with the DLT, which increases the average production cross-section-as one can deduce from figure 10(a). However, the evaluation of the relevance of such radiation sources for medical applications cannot ignore the quantification of the amount of radioisotopes potentially available with these sources. To evaluate so, we calculated the expected activity (A) as a function of the irradiation time of the boron target as:

$$A = RR \cdot N_\mathrm{p} \cdot Y \cdot \left(1 - \mathrm{e}^{-\lambda t}\right) \,, \tag{14}$$

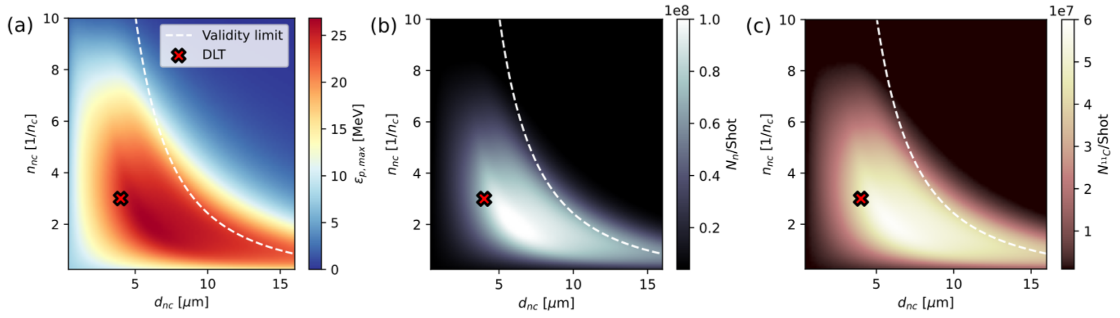

Figure 11. DLT performances as a function of the near-critical layer density n_{c} and thickness d_{nc} evaluated with model developed by Pazzaglia *et al* [13]. In (a) the maximum proton energy is reported, while in (b) and (c) the number of generated neutrons and produced ^{11}C radioisotopes per laser shot are presented, respectively. The x-shaped marker identifies the same DLT condition considered for MC simulations, and the dashed white line coincides with the validity limit of the model.

where $\lambda = \ln(2)/t_{1/2}$ is the decay constant, RR is the laser repetition rate, and N_{p} is the number of protons accelerated per shot. The results are reported in figure 10(c) as yellow and red lines for the BT and DLT, respectively. The minimum activity required for preclinical studies is usually set to 10.0 MBq and is shown in the plot as a shaded region in water-marine colour. With the studied laser parameters, the DLT configuration could allow one to achieve this value in less than 4 minutes of continuous shots at the nominal 10 Hz repetition rate. On the other hand, a saturation value of 8.5 MBq is expected with solid foils, which do not guarantee a sufficient amount of ^{11}C for preclinical studies. For comparison, results from Tayyab *et al* [121] and Peñas *et al* [122] are reported as dashed light and dark blue lines, respectively. The ^{11}C production yields were experimentally obtained with 150 TW (2.5 J pulse energy, 10 Hz repetition rate) and 1 PW (25 J pulse energy, 1 Hz repetition rate) lasers. The activities extrapolated from the experimental results are comparable with those retrieved from our simulations.

5.3. Nuclear reaction yields as a function of DLT foam properties

The applications investigated in the previous sections make use of proton-induced nuclear reactions, where the shared quantity of interest is the number of reactions per laser shot $N/Shot$. Although the use of MC simulations allows for a robust evaluation of the performance achievable with solid foils and DLTs, $N/Shot$ can be rapidly estimated through a simplified modelling approach. It is based on the use of the model described in section 3.1 and developed by Pazzaglia *et al* [13] to determine the properties of the accelerated protons as a function of the laser and DLT parameters. Once the proton spectrum $\mathrm{d}N_{\mathrm{p}}/\mathrm{d}\epsilon_{\mathrm{p}}$ is known, we can evaluate $N/Shot$ by taking into account the mass stopping power $S(E)$ of the material and the cross section $\sigma(E)$ associated with the nuclear process (see figure 10(a)) using the following formula:

$$\frac{N}{Shot} = \frac{N_{\mathrm{Av}}}{m_{\mathrm{A}}} f \int_{0}^{\epsilon_{\mathrm{p,max}}} \frac{\mathrm{d}N_{\mathrm{p}}}{\mathrm{d}\epsilon_{\mathrm{p}}} \int_{0}^{E} \frac{\sigma(E)}{S(E)} \mathrm{d}E \mathrm{d}\epsilon_{\mathrm{p}} \,, \tag{15}$$

where N_{Av} is the Avogadro's number, m_{A} and f are the atomic mass and isotopic abundance of the isotope involved in the nuclear reaction, respectively. This approach allows us to estimate the performance in terms of generated neutrons and produced radioisotopes as a function of the density and thickness of the near-critical layer at fixed laser parameters.

We consider the same laser parameters described in section 5 and the same substrate thickness of 1.5 μm. By exploiting the model, we evaluate the maximum proton energy and electron temperature in the 0–10 n_{c} density and the 0–16 μm thickness ranges for the near-critical layer. The calculated maximum proton energy is reported in figure 11(a). The dotted white line identifies the upper limit of validity of the model as $d_{\mathrm{nc}} < 2l_{\mathrm{f}}$ [13], where l_{f} is the self-focusing focal length. Note that the model estimates $\epsilon_{\mathrm{p,max}}$ equal to 8 MeV and 20 MeV for the solid foil and DLT (the x-shaped marker) in the same experimental conditions adopted in [31] and reproduced with PIC simulations (see section 4.1). These values are coherent with experimental and numerical results.

We linearly fit the number of protons accelerate per shot N_{p} for all target parameters considering the values of $\epsilon_{\mathrm{p,max}}$ and N_{p} with the solid foil and DLT adopted in the MC simulations. The energy spectra $\mathrm{d}N_{\mathrm{p}}/\mathrm{d}\epsilon_{\mathrm{p}}$ are calculated with equation (4.1), and the number of nuclear reactions for neutron generation and ^{11}C production is evaluated with equation (5.3) where the $S(E)$ is retrieved from SRIM tables [129].

The numbers of generated neutrons and produced radioisotopes as a function of near-critical layer thickness and density are reported in figures 11(a) and (b) respectively.

They reflect the trend of the maximum energy, and the near-critical layer has a beneficial effect starting from a thickness of approximately 2 μm. For thickness values larger than approximately 5 μm, even sub-critical densities allow for an enhancement of the proton energy and of the number of nuclear reactions. Moreover, for densities exceeding approximately $7\,n_c$, within the range of validity of the model, a drastic drop in performance is observed, bringing the results back to values comparable to those of a solid foil. Overall, it can be observed that there exists a region in parameter space for which the DLT is effective in increasing the number of nuclear reactions. This suggests that DLTs can represent a robust solution for enhancing the performance of the applications, even when accounting for possible uncertainties in the near-critical layer parameters.

5.4. Elemental mapping with FF-PIXE

Among the non-destructive elemental analysis techniques, PIXE is commonly exploited owing to its high sensitivity to low concentration (up to the 10 s of part per billion level) elements [130]. In its most common configuration, PIXE exploits MeV-energy protons to irradiate materials and induce the emission of characteristic x-rays from the materials themselves. The emitted x-rays are collected through a detector, which enables x-ray spectroscopy, allowing, through models, for the determination of the elemental composition of the irradiated sample. Beyond its applications in industry and environmental monitoring [131–133], PIXE is of particular interest for heritage science analyses due to its non-destructive nature combined with the high sensitivity [134–138]. In this context, the need for compact and possibly transportable instrumentation makes laser-driven sources a promising alternative to conventional accelerators. Proof-of-principle experiments have shown that laser-driven PIXE is capable of identifying the elements present in a material, determining their concentration, and performing stratigraphic analysis of non-homogeneous structures [139–146]. Here, the use of advanced targets, such as DLTs, could further advance configurations based on this technique, by enabling more compact and more efficient setups [58, 62].

One advanced PIXE scheme-yet unexplored in the context of laser-based accelerators-involves the irradiation of samples whose composition varies across the surface with large beam spots (as is the case for many artistic and archaeological artifacts). The x-rays collection is performed by spatially separating the contributions, allowing one to observe (at a 10 s of μm spatial resolution) the spatial variation of the sample composition. As it usually happens in laser-driven PIXE experiments, x-rays are detected with scientific CCD cameras that enable spatial discrimination of photons incident on different pixels of the sensor. However, in this case, between the sample and the CCD, a straight-shaped polycapillary lens is placed to filter out x-rays emitted at non-orthogonal angles to the surface. By combining the information on the energy and position of the x-rays detected by the CCD, the signal can be analysed generating a bi-dimensional map of the sample composition across its surface. This x-ray detection configuration was already proved successful in x-ray fluorescence spectroscopy measurements [147, 148] and in PIXE measurements with conventional accelerators [149, 150], but it has poorly been tested with laser-driven proton sources. The aim of this section is to investigate this approach in laser-driven PIXE, using solid foils and nanofoam-based DLTs. A representation of the scheme described above and of the geometry implemented in the MC simulation is shown in figure 12(a).

The simulated sample consists of a chequerboard matrix of alternating copper and iron with a 1 mm pitch. The straight polycapillary lens has a diameter of 1 cm and a length of 2.5 cm. It is simulated as a honeycomb matrix with hexagonal channels having a distance of 15 μm between two opposite vertices. The hexagons are separated by 3 μm-thick borosilicate-glass walls. The channel cross-section size is chosen as a compromise between the heaviness of the simulation in terms of geometry complexity and closeness to realistic values (the polycapillary-channel diameter is generally a few micrometres). The bundle is embedded in an aluminium cylinder, and a protective Mylar film with a thickness of 3 μm was placed in front of the face oriented toward the sample. The distances between the sample and the film, and between the film and the bundle front face are 2.25 cm and 0.5 cm, respectively. At a distance of 0.75 cm from the rear surface of the bundle, a square CCD screen with a side length of 1.2 cm is placed. The CCD energy resolution is modelled considering 100 eV-FWHM peak broadening. Thus, when a x-ray impact on the screen, the stored energy is sampled according to a Gaussian distribution with mean value equal to the incident x-ray energy and standard deviation equal to $\mathrm{FWHM}/(2\sqrt{2\log 2})$.

The simulation requires the correct description of the polycapillary. In fact, x-rays impacting the surfaces of the polycapillary channels at sufficiently small angles can undergo specular reflections due to total reflections caused by the change in the refractive index. Therefore, the `G4XrayReflection` process is introduced to treat this phenomenon in Geant4 for pure elemental materials. The implemented

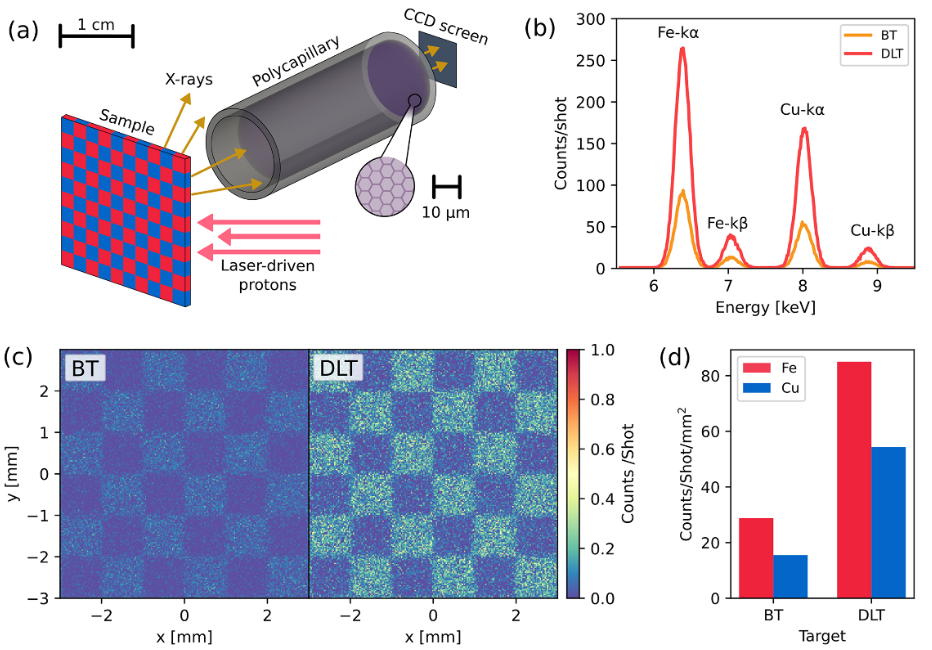

Figure 12. Laser-driven FF-PIXE with BTs and DLTs. In (a), laser-driven FF-PIXE setup and MC simulation geometry. In (b), the energy spectra of the x-rays incident on the CCD with BT (yellow) and DLT (red). In (c), the maps of the Cu x-ray number incident on the CCD per shot with BT (left) and DLT (right). In (d), the number of x-rays detected per unit shot and CCD active surface.

reflection model is the same described by Henke *et al* [151]. It exploits the anomalous scattering coefficients ($f1$ and $f2$) as a function of the incident photon energy, and they are reported in the *G4EMLOW* dataset distributed with Geant4. Since polycapillary lenses are usually made of borosilicate glass, here, we evaluate the complex refractive index n as if the glass was a perfect mixture through equation (16):

$$n = 1 - \frac{r_e \lambda^2 N_A \rho}{2\pi A} \sum_j n_j \left(f_{1,j} + i f_{2,j}\right) , \tag{16}$$

where r_e is the classical electron radius, λ is the wavelength of incident radiation, N_A is the Avogadro number, ρ is the density of the material, A is the atomic weight, n_j is the atomic fraction of the j-th element. Then, we implement a user-defined physical process class that takes advantage of the same model used for `G4XrayReflection` [151], but considering the calculated refractive index of the glass. We kept the same electromagnetic physics module and production cuts as in the simulations of the previous sections. Moreover, we activate the PIXE, fluorescence and Auger processes, and we apply a cross-section biasing to the x-ray emission process to speed up the simulation. As in the other sections, we perform two simulations considering the proton spectra obtained with BTs and DLTs reported in figure 10(a). For each simulation, 7×10^9 primary protons are launched, and the results are rescaled to the number of protons per shot.

Figure 12(b) shows the total x-ray spectra incident on the CCD screen. The use of DLTs increases of approximately 3 times the number of x-rays per laser shot compared to the BTs. To test laser-driven FF-PIXE, we tracked the x-rays associated with copper (i.e. those in an energy range between 7.5 and 9.5 keV). Since each x-ray in this energy range is associated with the pixel of the CCD where it interacted, we were able to track also the position within the assumed pixel size (we assumed a spatial discretisation of 30 μm). We mapped in this way the number of Cu x-rays per shot as a function of position on the CCD screen. The result is shown in figure 12(c) for both the solid foil and the DLT configurations. Firstly, one can notice that, as expected due to the presence of the polycapillary lens, the distribution of Cu x-rays incident on the CCD qualitatively reflects the distribution of the element within the sample. However, in regions where Cu should be absent, there is still a background of x-rays associated with it. This effect can be related to the non-ideal behaviour of the polycapillary and to the gap between its exit surface and the CCD screen. This effect can nevertheless be mitigated by using a polycapillary with a smaller channel diameter. While a 15 μm diameter was used in these simulations to limit the number of volumes in the geometry and reduce the computational costs, x-ray optics with few-micrometre-channel diameter are available.

As one could expect by the increase in the total x-rays produced with the DLT, the number of Cu x-rays detected at different points of the CCD is consistently higher when the DLT is used. This is qualitatively pointed out by the colour scale in figure 12(c), that shows an overall increased signal for the DLT x-ray map. Quantitatively, the number of x-rays per unit area per shot associated with the two simulations is reported in figure 12(d). As for neutron generation and radioisotope production, the simulations suggest that the laser-driven FF-PIXE could benefit from the use of advanced DLT targets in terms of efficiency, either reducing the measurement times or the laser parameters at fixed yield.

6. Nanofoams in laser-driven nuclear fusion

The improved laser-target coupling promoted by low-density porous materials has made foams attractive also in the field of ICF. Considering the direct-drive scheme, low-Z plastic foams produced via chemical methods or 3D printing have been considered. They can smooth laser energy inhomogeneities [152], enhance the absorption efficiency [153], and increase the ablation loading [154]. Mid-Z materials like high-density carbon (HDC) have shown improved target performances both in the direct and indirect schemes [155, 156], reducing laser plasma instabilities. Carbon nanofoams, as low-density mid-Z materials, are, thus, a promising candidate that is being currently explored, as highlighted in section 3.2. Low-density foam materials have also gained a substantial interest in the field of proton-boron fusion. Here, laser-driven in-target schemes are the most promising [157]. Thus, nanofoams can be employed as a mean to overcome the inherent limitations of the reaction in terms of cross-section and, thus, to increase the alpha particle yield [158–161]. In the following, our most recent results in this direction are outlined: we focus on a novel method for hydrogen-enriched boron nanofoams production, and their properties as target materials for proton-boron fusion experiments.

6.1. Boron and polymer nanofoams for proton-boron fusion

While still a small portion of the research efforts devoted to ICF, the proton-boron reaction has never lost the interest of scientists [157, 162, 163] and private companies [164] alike, due to the unique absence of neutrons among the reaction products. Although the research interest was driven by the potential for energy-related applications-on which the focus of private companies lies-, the scientific interest is broader, encompassing laser-driven alpha-particle sources, ion-beam applications, and fundamental nuclear and plasma physics [162, 163, 165–167]. When compared to the more established deuterium-tritium reaction, the main drawback stems from the substantially lower cross-section which significantly hinders a thermonuclear approach. Laser-driven schemes, in the in-target approach or pitcher-catcher configuration, can be instrumental in overcoming this limitation, with their signature non-equilibrium energy transfer processes. Here, nano- and micro-structured materials and foams can be particularly advantageous in enhancing laser-matter interaction and, thus, fusion reactions and alpha-particle yield. Indeed, different target configurations have been proposed and investigated in recent years, from plasma polymers coupled with boron nitride (BN) [158] to boranes and their micro and nanostructures [159, 160]. However, when limiting the discussion to the in-target approach, the ideal target should contain both boron and protons (hydrogen) in abundant quantities. This characteristic is not straightforward by itself: boron-hydrogen compounds are mostly gaseous, chemically unstable, or toxic-with only few exceptions. Owing to these limitations, the most commonly used target material in proton-boron fusion experiments is BN, a solid ceramic compound in which a small percentage of hydrogen is present as a by-product of its fabrication process [157]. Alongside some surface hydrogen-containing impurities, this quantity is enough to promote a few fusion reactions. However, only the production of advanced targets can pave the way for the process optimisation. Here, hydrogen-enriched targets, containing both protons and boron in similar amounts in nanofoam configuration to enhance laser absorption, can be a strategy for achieving increased particle yields.

As introduced in section 2.1.2, polymer-based materials can be produced as nanofoams through fs-PLD, and can act as an efficient source of hydrogen-the main downside being the presence of a comparable amount of carbon atoms. The characteristic nanoparticle-assembled foam morphology can be distinguished in the top panels of figure 13(a), where a CH_2 foam obtained from a HDPE target is shown (20 μm thickness, 140 $\mathrm{mg\,cm^{-3}}$ density). The simplest improved target concept exploiting this nanofoam is its addition on top of a boron-containing solid target, such as BN-often the reference target in proton-boron fusion experiments. Another interesting possibility is a simple boron nanofoam target, which, unlike BN, is made of pure boron (with only $\approx$5% of oxygen due to oxidation). Determining to what extent hydrogen impurities, potentially increased due to the high porosity of the nanofoam material, can be sufficient in promoting p-B fusion reactions can be extremely useful for the process optimisation. A boron nanofoam of this kind (50 μm thickness, 100 $\mathrm{mg\,cm^{-3}}$ density) is shown in the second row of

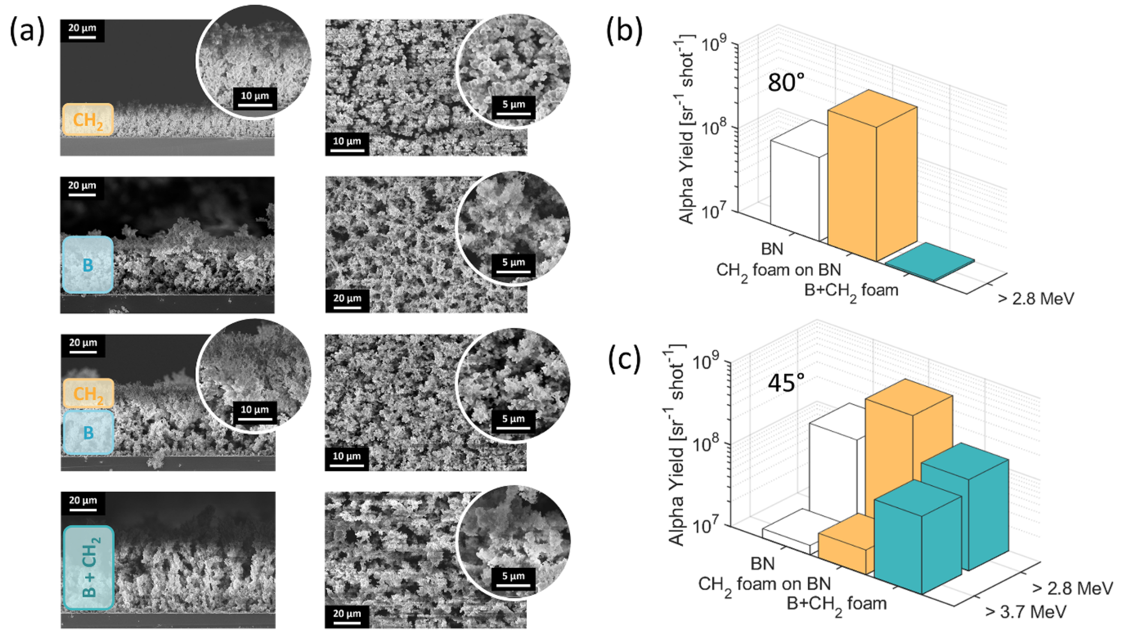

Figure 13. In (a), boron and polymer (CH$_2$) nanofoams produced in the framework of proton-boron fusion research are presented. Cross-section SEM micrographs are shown in the first column, with the corresponding plane-view on the side. The insets provide higher magnification details. From top to bottom: CH$_2$ foam, boron foam, stacked boron and CH$_2$ foam, mixed boron and CH$_2$ foam. In (b) and (c), the experimental results in terms of alpha particle yield for different targets, at 80° and 45° respectively, obtained at the Taranis experimental campaign [161].

figure 13(a). Lastly, the most interesting concept is a composite target, in which both boron and polymer foams are combined. Many are the possibilities within this concept. One possibility is shown in the third row of figure 13(a), where a layer of CH$_2$ foam of $\approx 15\,\mu$m is deposited on top of a boron nanofoam. In the inset of the cross-section image, the morphology transition between the two can be appreciated. A second approach consists of a mixed B-CH$_2$ nanofoam, that can be produced through fs-PLD co-deposition (refer to section 2.1.2 for details). An example of this foam is shown in the bottom row of figure 13(a). In this way, the target synthesis time is reduced, and the two p-B fusion reagents are better intermixed in the target. As one can observe in the SEM image, the morphology of the mixed nanofoam appears to be more compact and has a more pronounced vertical directionality, likely a consequence of the highly energetic HDPE ablated species. The mixed nanofoam has a density of 80 mg cm^{-3} and a thickness of 60 μm, with a C/B ratio of $\approx$0.7. Considering the direct nanoparticle emission of fs-PLD, it is reasonable to assume that the 2:1 H/C ratio of HDPE is retained, thus, leading to a H/B ratio of $\approx$1.4.

The performance of these nanofoam-based targets in proton-boron fusion is explored in an experimental campaign at the TARANIS laser facility (Queen's University, Belfast) [161]. TARANIS [168] is a 10-TW laser system, operating at 1053 nm, providing up to 10 J pulses in 800 fs with an intensity of 2×10^{19} W cm^{-2} over the 5.1 μm focused spot. The laser also features a non-negligible nanosecond prepulse (5×10^{-7} contrast ratio). The longer pulse duration (with respect to the femtosecond lasers common in laser-driven particle acceleration), together with the presence of a prepulse, can be advantageous to prolong laser-matter interaction and promote fusion reaction, provided a proper target design. Indeed, this is the reason for the higher densities-with respect to the critical density-chosen for the nanofoams produced for this experiment. In all the nanofoam samples, a polypropylene substrate is used. Nuclear track detectors (CR-39) are exploited as the main diagnostic to evaluate the alpha particle yield, together with a differential filtering scheme useful to gain insight into alpha particle energies and the presence of heavier ions. The alpha particle yield for different types of targets is shown in figures 13(b) and (c), for two different positions: high angles (80°) and low angles (45°) from the target normal, respectively. The BN target is included as a reference point, showing a yield within the order of 10^8 alphas per steradian per shot. The results for the simple boron nanofoam are not reported in the figure, since they are below the sensitivity of the nuclear track detector setup. This highlights the low natural content of hydrogen in these nanofoams, underlining the need for hydrogen enrichment. Promising results emerge, instead, from the composite targets obtained by combining a BN substrate with a CH$_2$ nanofoam. The yield is increased multiple times in comparison with pure BN, confirming the validity of the approach. The mixed boron and CH$_2$ nanofoam also provides interesting results, with some notable differences. At higher angles, the yield is strongly suppressed. This effect can be attributed to the shielding capabilities of the surrounding foam on the alpha-particles produced in the central laser-interaction region of the target. Moreover, the presence of a significantly larger high-energy alpha particle fraction, together with a substantial population of heavy ions in the accelerated species, can be an indication of the CE of nanoparticles as one of the main mechanisms driving proton-boron fusion in this class of materials.

7. Conclusion and perspectives

In this paper, we have presented our recent results and advancements on PLD nanofoam targets and their use in LPI experiments and related applications. The fundamental idea is that precise control over the nanofoam properties offers better control over the laser-target coupling, resulting in an enhancement of the laser-driven sources of particles and radiation or ablation loading efficiency.

To this aim, a key element is the fabrication of advanced targets with controlled density, thickness, and nanoscale structure. PLD provides this control with good reproducibility. In parallel, we have improved the physical picture of the relevant interaction regimes, linking foam morphology and density to the mechanisms involved in laser-plasma coupling. A main focus has been on near-critical nanofoams in DLTs for ion acceleration. Modelling and experiments indicate that a low-density foam in front of a micrometric foil increases electron heating and shifts the proton spectrum toward higher energy and charge. This improvement also supports advances in the production of secondary radiation, such as bremsstrahlung and synchrotron-like radiation, neutron production via (p,n) reactions, emission of characteristic x-rays, and production of radioisotopes. As a consequence, we have shown that DLTs are extremely beneficial for applications of laser-driven radiation sources in many fields, including material characterisation techniques (e.g. FF-PIXE, FNAA, FNRR) and medical applications (production of short-lived radioisotopes for PET).

We have also addressed nanofoam targets for nuclear fusion research. In the context of direct-drive ICF, hydrodynamic simulations of PLD carbon foams used as ablators show that the foam nanostructure affects the pressure at the shock front, increasing the ablation loading compared to standard targets. This points to foam ablators as a potential route to improve shock delivery in direct-drive schemes. In addition, we explored nanofoam concepts for proton-boron fusion in the in-target scheme. Recent experiments using polymer and boron-polymer nanofoams produced by PLD demonstrate alpha-particle fluxes competitive with the state of the art at moderate laser energy, indicating that material design at the nanofoam level is a key lever for better fusion performance.

When placing these results in the broader context of foam-based targets, it is worth commenting on the specific features of PLD nanofoams compared with alternative production methods, such as chemical synthesis and additive manufacturing. Chemically produced foams can be fabricated cost-effectively over large areas and volumes but are often restricted to specific elements, offer limited control at the nanoscale, and may rely on toxic precursors or by-products. Additive manufacturing enables complex three-dimensional geometries and precise morphology control at the tens to hundreds of micrometres scale, which is advantageous when the macroscopic hydrodynamic response or capsule geometry is the main design constraint; on the other hand it is difficult to approach the sub-wavelength scale and the flexibility in elemental composition is limited. PLD nanofoams provide a complementary alternative: they offer tuneable control down to the nanoscale, can be grown on different solid substrates or combined in layered structures, with a high degree of flexibility in the choice of materials. At the same time, PLD offers limited deposition area and lower throughput than chemical synthesis or 3D printing, and the deposition infrastructure can be rather complex. As such, PLD nanofoams are especially suited to both fundamental studies and applications in which precise control over the laser-target coupling is required, while conventional alternatives remain preferable for large-scale production of simple and thick targets, or for three-dimensional arrangements where morphology matters only at the hundreds-of-micrometres scale.

An additional perspective concerns doping strategies in PLD nanofoam targets. The same level of control that PLD offers over density and morphology can in principle be extended to the introduction of selected dopants and compositional gradients. This could enable built-in diagnostics, for example by embedding trace elements with well separated characteristic x-ray lines to infer plasma temperature and density, as well as targets where two nuclides are co-located to favour specific in-target nuclear reactions.

More generally, the results show that nanofoams for LPI should not be considered just as a single-purpose solution but rather a common platform to control the laser-target interaction regime. A comprehensive and integrated view of the whole process, combining theoretical and experimental development in nanofoam synthesis, the laser-nanostructure interaction across different intensity regimes, and application design–while accounting for physical and technological limits–is, thus, essential to unlock the full potential of this valuable tool for the advancement of the research field of LPI.

Acknowledgments

Part of this research has been carried out at the ELI Beamlines Facility, a European user facility operated by the Extreme Light Infrastructure ERIC. Authors thank the ELI Beamlines staff for the support during the experiment. Part of this research has been carried out at the Laboratoire pour l'Utilisation des Lasers Intenses (LULI, CNRS, CEA, Sorbonne Université, École Polytechnique, Institut Polytechnique de Paris, UMR 7605, F-91128, Palaiseau, France) and at its research infrastructure Apollon during the experimental campaign "Nonlinear Inverse Compton Scattering from double-layer targets at Apollon 1PW" with principal investigator Dr Livia Lancia. The authors thank the LULI and Apollon team for their support. Part of this research has been carried out at the Centre for Light-Matter Interactions, Queen's University Belfast (QUB), Belfast, UK. Authors thank the QUB team for their support. The authors also thank Fabrizio Consoli and Mattia Cipriani (ENEA Centro Ricerche Frascati) for insightful discussion. This work used the open-source PIC code SMILEI. The authors are grateful to all SMILEI contributors and the SMILEI-dev team for their support. Simulations were performed on the Galileo100 machine hosted at CINECA, Italy, using resources from the TRIDENT project (ID No. HP10C0LZ9X), the SUPERG project (ID No. HP10C9OU0Y) and from the agreement between the Department of Energy at Politecnico di Milano and the CINECA consortium (Casalecchio di Reno, Italy), and on the Irene-Joliot-Curie machine hosted at TGCC, France, using resources from GENCI-TGCC (Grant No. A0170507678). We acknowledge the CINECA award under the ISCRA initiative and the GENCI-TGCC award for the availability of high-performance computing resources and support. This project has received funding from the European Research Council (ERC) under the European Union's Horizon 2022 research and innovation program (PoC-PANTANI Grant Agreement No. 101069171. This work received support from COST Action CA21128-PROBONO 'PROton BOron Nuclear fusion: from energy production to medical applicatiOns', supported by COST (European Cooperation in Science and Technology). The authors also acknowledge the financial support of the European Union Next Generation EU and Italian Ministry of University and Research as part of the PRIN 2022 program, project 'Nanomaterials for Fusion: experimental and modelling of nanostructured materials and plasma-material interactions for inertial & magnetic confinement fusion' (project ID: 2022N5JBHT, CUP D53D23002840006). Kevin Ambrogioni acknowledges the Italian Ministry of University and Research (MUR) under the National Recovery and Resilience Plan (PNRR), Mission 4, Component 1, Investment 3.4, through the Ministerial Decree n.118 for partially funding this research. Maria Sole Galli De Magistris acknowledges the Italian Ministry of University and Research (MUR) under the National Recovery and Resilience Plan (PNRR), Mission 4, Component 2, Investment 3.3, through the Ministerial Decree n.117 for partially funding this research.

Data availability statement

The data that support the findings of this study will be openly available following an embargo at the following URL/DOI: https://polimi365-my.sharepoint.com/personal/10 277 594_polimi_it/_layouts/15/onedrive.aspx?id = %2Fpersonal%2F10277594%5Fpolimi%5Fit%2FDocuments%2FDataRepository%5FPPCF%2D105455&ga = 1 [169].

PIC simulation parameters available at https://doi.org/10.1088/1361-6587/ae44c8/data1.

Author contributions

Alessandro Maffini 0000-0002-3388-5330
Conceptualization (lead), Funding acquisition (supporting), Investigation (equal), Methodology (equal), Supervision (equal), Writing – original draft (equal)

Kevin Ambrogioni 0009-0000-0039-0895
Investigation (equal), Methodology (equal), Visualization (equal), Writing – original draft (equal)

David Dellasega 0000-0002-7389-9307
Investigation (equal), Methodology (equal)

Marta Galbiati 0000-0001-6514-3887
Investigation (equal), Methodology (equal), Visualization (equal), Writing – original draft (equal)

Maria Sole Galli de Magistris 0009-0002-3366-7840
Investigation (equal), Methodology (equal), Visualization (equal), Writing – original draft (equal)

Francesco Gatti 0000-0001-6894-1155
Investigation (equal), Methodology (equal)

Matteo Iaccarino 0009-0002-4430-8616
Investigation (equal), Methodology (equal), Visualization (equal), Writing – original draft (equal)

Claudia Mallimaci
Investigation (equal), Methodology (equal)

Francesco Mirani 0000-0002-9789-0075
Conceptualization (supporting), Investigation (equal), Methodology (equal), Visualization (equal), Writing – original draft (equal)

Davide Orecchia 0000-0003-3900-5928
Investigation (equal), Methodology (equal), Visualization (equal), Writing – original draft (equal)

Valeria Russo 0000-0001-9543-0422
Investigation (equal), Methodology (equal)

Davide Vavassori 0000-0003-1279-3645
Investigation (equal), Methodology (equal)

Matteo Passoni 0000-0002-7844-3691
Funding acquisition (lead), Investigation (equal), Methodology (equal), Supervision (equal)

References

[1] Ghosh S *et al* 2024 Ballistic-aggregated carbon nanofoam in target-side of pulsed laser deposition for energy storage applications *ChemSusChem* **17** 755

[2] Ghosh S, Righi M, Macrelli A, Goto F, Agozzino M, Bussetti G, Russo V, Bassi A Li and Casari C S 2025 Low-density functionalized amorphous carbon nanofoam as binder-free thin-film supercapacitor electrode *Carbon Trends* **20** 100516

[3] Dutta A, Morstein C E, Rahaman M, Cedeño López A and Broekmann P 2018 Beyond copper in CO_2 electrolysis: effective hydrocarbon production on silver-nanofoam catalysts *ACS Catal.* **8** 8357–68

[4] Salama A, Abouzeid R, Leong W S, Jeevanandam J, Samyn P, Dufresne A, Bechelany M and Barhoum A 2021 Nanocellulose-based materials for water treatment: adsorption, photocatalytic degradation, disinfection, antifouling and nanofiltration *Nanomaterials* **11** 3008

[5] Liu X, Wang S, Sun C, Liu H, Stevens L, Dwomoh P K and Snape C 2020 Synthesis of functionalized 3D microporous carbon foams for selective CO_2 capture *Chem. Eng. J.* **402** 125459

[6] Löbmann K, Wohlert J, Müllertz A, Wågberg L and Svagan A J 2017 Cellulose nanopaper and nanofoam for patient-tailored drug delivery *Adv. Mater. Interfaces* **4** 1600655

[7] Fedeli L, Formenti A, Cialfi L, Pazzaglia A and Passoni M 2018 Ultra-intense laser interaction with nanostructured near-critical plasmas *Sci. Rep.* **8** 3834

[8] Rosmej O N *et al* 2019 Interaction of relativistically intense laser pulses with long-scale near critical plasmas for optimization of laser based sources of MeV electrons and gamma-rays *New J. Phys.* **21** 043044

[9] Pukhov A and Meyer-Ter-Vehn J 1996 Relativistic magnetic self-channeling of light in near-critical plasma: three-dimensional particle-in-cell simulation *Phys. Rev. Lett.* **76** 3975–8

[10] Pukhov A, Sheng Z-M and Vehn J M-ter 1999 Particle acceleration in relativistic laser channels *Phys. Plasmas* **6** 2847–54

[11] Sgattoni A, Londrillo P, MacChi A and Passoni M 2012 Laser ion acceleration using a solid target coupled with a low-density layer *Phys. Rev. E* **85** 405

[12] Arefiev A V, Khudik V N, Robinson A P L, Shvets G, Willingale L and Schollmeier M 2016 Beyond the ponderomotive limit: direct laser acceleration of relativistic electrons in sub-critical plasmas *Phys. Plasmas* **23** 24

[13] Pazzaglia A, Fedeli L, Formenti A, Maffini A and Passoni M 2020 A theoretical model of laser-driven ion acceleration from near-critical double-layer targets *Commun. Phys.* **3** 7

[14] Di Piazza A, Müller C, Hatsagortsyan K Z and Keitel C H 2012 Extremely high-intensity laser interactions with fundamental quantum systems *Rev. Mod. Phys.* **84** 1177–228

[15] Phuoc K T, Corde S, Thaury C, Malka V, Tafzi A, Goddet J P, Shah R C, Sebban S and Rousse A 2012 All-optical Compton gamma-ray source *Nat. Photon.* **6** 308–11

[16] Formenti A, Galbiati M and Passoni M 2024 Three-dimensional particle-in-cell simulations of laser-driven multiradiation sources based on double-layer targets *Phys. Rev. E* **109** 206

[17] Galbiati M, Ambrogioni K, Monaco L F C, De Magistris M S G, Orecchia D, Mirani F, Maffini A and Passoni M 2025 Numerical proof-of-concept of nanofoam-based targets for proton acceleration and high-energy photon and positron generation in strong fields

[18] Macchi A, Borghesi M and Passoni M 2013 Ion acceleration by superintense laser-plasma interaction *Rev. Mod. Phys.* **85** 751–93

[19] Hatchett S P *et al* 2000 Electron, photon and ion beams from the relativistic interaction of Petawatt laser pulses with solid targets *Phys. Plasmas* **7** 2076–82

[20] Gus'Kov S Y, Cipriani M, De Angelis R, Consoli F, Rupasov A A, Andreoli P, Cristofari G and Di Giorgio G 2015 Absorption coefficient for nanosecond laser pulse in porous material *Plasma Phys. Control. Fusion* **57** 4

[21] Cipriani M, Gus'kov S Y, Consoli F, De Angelis R, Rupasov A A, Andreoli P, Cristofari G and Di Giorgio G 2020 Hydrodynamics and transport processes in porous materials under terawatt laser irradiation *J. Instrum.* **15** C10003

[22] Willingale L, Nilson P M, Thomas A G R, Bulanov S S, Maksimchuk A, Nazarov W, Sangster T C, Stoeckl C and Krushelnick K 2011 High-power, kilojoule laser interactions with near-critical density plasma) *Phys. Plasmas* **18** 056706

[23] Venkatakrishnan K, Vipparty D and Tan B 2011 Nanofibre fabrication by femtosecond laser ablation of silica glass *Opt. Express* **19** 15770–6

[24] Grant-Jacob J A, Mills B and Eason R W 2014 Parametric study of the rapid fabrication of glass nanofoam via femtosecond laser irradiation *J. Phys. D: Appl. Phys.* **47** 055105

[25] Grant-Jacob J, Mackay B S, Baker J, Xie Y, McDonnell M D T, Heath D, Praeger M, Eason R W and Mills B 2019 Patterned nanofoam fabrication from a variety of materials via femtosecond laser pulses *Mater. Sci. Appl.* **10** 186–96

[26] Andreev A, Platonov K, Braenzel J, Lübcke A, Das S, Messaoudi H, Grunwald R, Gray C, McGlynn E and Schnürer M 2015 Relativistic laser nano-plasmonics for effective fast particle production *Plasma Phys. Control. Fusion* **58** 014038

[27] Lübcke A, Andreev A A, Höhm S, Grunwald R, Ehrentraut L and Schnürer M 2017 Prospects of target nanostructuring for laser proton acceleration *Sci. Rep.* **7** 44030

[28] Shepelin N, Tehrani Z, Ohannessian N, Schneider C, Pergolesi D and Lippert T 2023 A practical guide to pulsed laser deposition *Chem. Soc. Rev.* **52** 03

[29] Maffini A, Pazzaglia A, Dellasega D, Russo V and Passoni M 2022 *Production of Carbon Nanofoam by Pulsed Laser Deposition on Flexible Substrates* (Springer) pp 135–57

[30] Passoni M *et al* 2016 Toward high-energy laser-driven ion beams: nanostructured double-layer targets *Phys. Rev. Accel. Beams* **19** 301

[31] Prencipe I *et al* 2021 Efficient laser-driven proton and bremsstrahlung generation from cluster-assembled foam targets *New J. Phys.* **23** 093015

[32] Maffini A, Cipriani M, Orecchia D, Ciardiello V, Formenti A, Consoli F and Passoni M 2023 Numerical study of carbon nanofoam targets for laser-driven inertial fusion experiments *Laser Part. Beams* **2023** 430

[33] Stubenrauch C, Menner A, Bismarck A and Drenckhan W 2018 Emulsion and foam templating-promising routes to tailor-made porous polymers *Angew. Chem. Int. Edn.* **57** 10024–32

[34] Zhao H, Zhou M, Wen L and Lei Y 2015 Template-directed construction of nanostructure arrays for highly-efficient energy storage and conversion *Nano Energy* **13** 790–813

[35] Liu Y, Goebl J and Yin Y 2013 Templated synthesis of nanostructured materials *Chem. Soc. Rev.* **42** 2610–53

[36] Wu D, Xu F, Bin S, Fu R, He H and Matyjaszewski K 2012 Design and preparation of porous polymers *Chem. Rev.* **112** 3959–4015

[37] Feng H, Lu X, Wang W, Kang N-G and Mays J W 2017 Block copolymers: synthesis, self-assembly and applications *Polymers* **9** 494

[38] Wiste T, Maliuk O, Tikhonchuk V, Lastovicka T, Homola J, Chadt K and Weber S 2023 Additive manufactured foam targets for experiments on high-power laser-matter interaction *J. Appl. Phys.* **133** 650

[39] Maffini A, Orecchia D, Pazzaglia A, Zavelani-Rossi M and Passoni M 2022 Pulsed laser deposition of carbon nanofoam *Appl. Surf. Sci.* **599** 153859

[40] Khalenkov A M, Borisenko N G, Kondrashov V N, Merkuliev Y A, Limpouch J and Pimenov V G 2006 Experience of micro-heterogeneous target fabrication to study energy transport in plasma near critical density *Laser Part. Beams* **24** 283–90

[41] Reverchon E and Cardea S 2007 Production of controlled polymeric foams by supercritical co_2 *J. Supercrit. Fluids* **40** 144–52

[42] Tony T and Arvind A 2021 A facile and scalable approach in the fabrication of tailored 3d graphene foam via freeze drying *Materials* **14** 864

[43] Maffini A, Pazzaglia A, Dellasega D, Russo V and Passoni M 2019 Growth dynamics of pulsed laser deposited nanofoams *Phys. Rev. Mater.* **3** 404

[44] Orecchia D, Maffini A, Zavelani-Rossi M and Passoni M 2024 Versatile synthesis of nanofoams through femtosecond pulsed laser deposition *Small Struct.* **5** 60

[45] Ashfold M N R, Claeyssens F, Fuge G M and Henley S J 2004 Pulsed laser ablation and deposition of thin films *Chem. Soc. Rev.* **33** 23–31

[46] Rethfeld B, Ivanov D S, Garcia M E and Anisimov S I 2017 Modelling ultrafast laser ablation *J. Phys. D: Appl. Phys.* **50** 193001

[47] Pazzaglia A, Maffini A, Dellasega D, Lamperti A and Passoni M 2019 Reference-free evaluation of thin films mass thickness and composition through energy dispersive x-ray spectroscopy *Mater. Charact.* **153** 92–102

[48] Chrisey D B, Piqué A, McGill R A, Horwitz J S, Ringeisen B R, Bubb D M and Wu P K 2003 Laser deposition of polymer and biomaterial films *Chem. Rev.* **103** 553–76

[49] Mercado A L, Allmond C E, Hoekstra J G and Fitz-Gerald J M 2005 Pulsed laser deposition vs. matrix assisted pulsed laser evaporation for growth of biodegradable polymer thin films *Appl. Phys. A* **81** 591–9

[50] Haider A J, Alawsi T, Haider M J, Taha B A and Marhoon H A 2022 A comprehensive review on pulsed laser deposition technique to effective nanostructure production: trends and challenges *Opt. Quantum Electron.* **54** 488

[51] Cao B Q, Lorenz M, Rahm A, von Wenckstern H, Czekalla C, Lenzner J, Benndorf G and Grundmann M 2007 Phosphorus acceptor doped ZnO nanowires prepared by pulsed-laser deposition *Nanotechnology* **18** 455707

[52] Zhang F, Arita M, Wang X, Chen Z, Saito K, Tanaka T, Nishio M, Motooka T and Guo Q 2016 Toward controlling the carrier density of Si doped Ga_2O_3 films by pulsed laser deposition *Appl. Phys. Lett.* **109** 102105

[53] Ham S, Ryu J, Lee H, Park S, Ghim Y-C, Hwang Y S and Chung K-J 2023 Estimation of plasma parameters of x-pinch with time-resolved x-ray spectroscopy *Matter Radiat. Extremes* **8** 036901

[54] Meakin P 2011 *Fractals, Scaling and Growth Far From Equilibrium* (Cambridge University Press)

[55] Witten T A and Sander L M 1981 Diffusion-limited aggregation, a kinetic critical phenomenon *Phys. Rev. Lett.* **47** 1400–3

[56] Sander L M 1986 Fractal growth processes *Nature* **322** 789–93

[57] Meakin P 1999 Historical introduction to computer models for fractal aggregates *J. Sol-Gel Sci. Technol.* **15** 97–117

[58] Passoni M *et al* 2020 Advanced laser-driven ion sources and their applications in materials and nuclear science *Plasma Phys. Control. Fusion* **62** 014022

[59] Stukowski A 2010 Visualization and analysis of atomistic simulation data with OVITO-the Open Visualization Tool *Modelling Simul. Mater. Sci. Eng.* **18** 015012

[60] Fedeli L, Mirani F, Maffini A, Formenti A, Pazzaglia A, Tentori A, Arioli F M, Dellasega D, Russo V and Passoni M 2018 Laser-plasma based hadron sources for materials science applications *45th EPS Conf. on Plasma Physics, EPS 2018* pp 1708–11

[61] Maffini A, Mirani F, Giovannelli A, Formenti A and Passoni M 2023 Laser-driven production with advanced targets of copper-64 for medical applications *Front. Phys.* **11** 23

[62] Maffini A *et al* 2023 Towards compact laser-driven accelerators: exploring the potential of advanced double-layer targets *EPJ Tech. Instrum.* **10** 15

[63] Tosca M *et al* 2024 Enhanced laser absorption and ion acceleration by boron nitride nanotube targets and high-energy PW laser pulses *Phys. Rev. Res.* **6** 26

[64] Mirani F *et al* 2025 Addressing the role of advanced targets for enhanced control of laser-driven hadron sources *Phys. Rev. Appl.* **24** 014017

[65] Margarone D *et al* 2018 Elimaia: A laser-driven ion accelerator for multidisciplinary applications *Quantum Beam Sci.* **2** 8

[66] Schillaci F *et al* 2022 The ELIMAIA laser-plasma ion accelerator: technological commissioning and perspectives *Quantum Beam Sci.* **6** 30

[67] Ma W *et al* 2019 Laser acceleration of highly energetic carbon ions using a double-layer target composed of slightly underdense plasma and ultrathin foil *Phys. Rev. Lett.* **122** 803

[68] Shekhanov S, Gintrand A, Hudec L, Liska R, Limpouch J, Weber S and Tikhonchuk V 2023 Kinetic modeling of laser absorption in foams *Phys. Plasmas* **30** 86

[69] Guo-Zheng S, Ott E, Lee Y C and Guzdar P 1987 Self-focusing of short intense pulses in plasmas *Phys. Fluids* **30** 526–32

[70] Sprangle P, Esarey E and Ting A 1990 Nonlinear theory of intense laser-plasma interactions *Phys. Rev. Lett.* **64** 2011–4

[71] Nicolaï P *et al* 2012 Experimental evidence of foam homogenization *Phys. Plasmas* **19** 70

[72] Langdon A B and Birdsall C K 1970 Theory of plasma simulation using finite-size particles *Phys. Fluids* **13** 2115–22

[73] Derouillat J *et al* 2018 Smilei: a collaborative, open-source, multi-purpose particle-in-cell code for plasma simulation *Comput. Phys. Commun.* **222** 351–73

[74] Fedeli L *et al* 2022 Pushing the frontier in the design of laser-based electron accelerators with groundbreaking mesh-refined particle-in-cell simulations on exascale-class supercomputers *SC22: Int. Conf. for High Performance Computing, Networking, Storage and Analysis* (IEEE Computer Society)

[75] Arber T D *et al* 2015 Contemporary particle-in-cell approach to laser-plasma modelling *Plasma Phys. Control. Fusion* **57** 1–26

[76] Alessandro M *et al* 2026 Supplementary material

[77] Max C E 1976 Strong self-focusing due to the ponderomotive force in plasmas *Phys. Fluids* **19** 74–77

[78] Jirka M, Vranic M, Grismayer T and Silva L O 2020 Scaling laws for direct laser acceleration in a radiation-reaction dominated regime *New J. Phys.* **22** 083058

[79] Babjak R, Willingale L, Arefiev A and Vranic M 2024 Direct laser acceleration in underdense plasmas with multi-PW lasers: A path to high-charge, GeV-class electron bunches *Phys. Rev. Lett.* **132** 1255001

[80] Tikhonchuk V T and Weber S 2024 Physics of porous materials under extreme laser-generated conditions *Matter Radiat. Extremes* **9** 46

[81] Grava J, Purvis M A, Filevich J, Marconi M C, Rocca J J, Dunn J, Moon S J and Shlyaptsev V N 2008 Dynamics of a dense laboratory plasma jet investigated using soft x-ray laser interferometry *Phys. Rev. E* **78** 403

[82] Fryxell B, Olson K, Ricker P, Timmes F X, Zingale M, Lamb D Q, Macneice P, Rosner R, Truran J W and Tufo H 2000 Flash: an adaptive mesh hydrodynamics code for modeling astrophysical thermonuclear flashes *Astrophys. J.* **131** 273–334

[83] Tzeferacos P, Fatenejad M, Flocke N, Graziani C, Gregori G, Lamb D, Lee D, Meinecke J, Scopatz A and Weide K 2015 Flash MHD simulations of experiments that study shock-generated magnetic fields *High Energy Density Phys.* **17** 24–31

[84] Ramis R, Schmalz R and Meyer-Ter-Vehn J 1988 MULTI - a computer code for one-dimensional multigroup radiation hydrodynamics *Comput. Phys. Commun.* **49** 475–505

[85] Rosmej O N *et al* 2025 Advanced plasma target from pre-ionized low-density foam for effective and robust direct laser acceleration of electrons *High Power Laser Sci. Eng.* **13** e3

[86] Hudec L, Gintrand A, Limpouch J, Liska R, Shekhanov S, Tikhonchuk V T and Weber S 2023 Hybrid ablation-expansion model for laser interaction with low-density foams *Phys. Plasmas* **30** 88

[87] Prencipe I *et al* 2017 Targets for high repetition rate laser facilities: Needs, challenges and perspectives *High Power Laser Sci. Eng.* **5** 18

[88] Snavely R A *et al* 2000 Intense high-energy proton beams from petawatt-laser irradiation of solids *Phys. Rev. Lett.* **85** 2945–8

[89] Maksimchuk A, Gu S, Flippo K, Umstadter D and Bychenkov A Y 2000 Forward ion acceleration in thin films driven by a high-intensity laser *Phys. Rev. Lett.* **84** 4108–11

[90] Clark E L *et al* 2000 Measurements of energetic proton transport through magnetized plasma from intense laser interactions with solids *Phys. Rev. Lett.* **84** 670–3

[91] Mora P 2003 Plasma expansion into a vacuum *Phys. Rev. Lett.* **90** 185002/1-185002/4

[92] Passoni M and Lontano M 2008 Theory of light-ion acceleration driven by a strong charge separation *Phys. Rev. Lett.* **101** 115001

[93] Formenti A, Maffini A and Passoni M 2020 Non-equilibrium effects in a relativistic plasma sheath model *New J. Phys.* **22** 053020

[94] Wilks S C, Langdon A B, Cowan T E, Roth M, Singh M, Hatchett S, Key M H, Pennington D, MacKinnon A and Snavely R A 2001 Energetic proton generation in ultra-intense laser-solid interactions *Phys. Plasmas* **8** 542–9

[95] Kluge T, Bussmann M, Schramm U and Cowan T E 2018 Simple scaling equations for electron spectra, currents and bulk heating in ultra-intense short-pulse laser-solid interaction *Phys. Plasmas* **25** 53

[96] Mackinnon A J, Sentoku Y, Patel P K, Price D W, Hatchett S, Key M H, Andersen C, Snavely R and Freeman R R 2002 Enhancement of proton acceleration by hot-electron recirculation in thin foils irradiated by ultraintense laser pulses *Phys. Rev. Lett.* **88** 2150061–4

[97] Sgattoni A, Fedeli L, Sinigardi S, Marocchino A, Macchi A, Weinberg V, and Karmakar A 2015 Optimising PICCANTE - an open source particle-in-cell code for advanced simulations on Tier-0 systems

[98] Mondal S *et al* 2018 Surface plasma attosource beamlines at ELI-ALPS *J. Opt. Soc. Am. B* **35** A93–A102

[99] Koch H W and Motz J W 1959 Bremsstrahlung cross-section formulas and related data *Rev. Mod. Phys.* **31** 920–55

[100] Stark D, Toncian T and Arefiev A 2016 Enhanced multi-mev photon emission by a laser-driven electron beam in a self-generated magnetic field *Phys. Rev. Lett.* **116** 5003

[101] Babjak R and Vranić M 2025 Betatron radiation emitted during the direct laser acceleration of electrons in underdense plasmas *Plasma Phys. Control. Fusion* **67** 085019

[102] Ritus V I 1985 Quantum effects of the interaction of elementary particles with an intense electromagnetic field *J. Sov. Laser Res.* **6** 497–617

[103] Bethe H A and Maximon L C 1954 Theory of bremsstrahlung and pair production. I. Differential cross section *Phys. Rev.* **93** 768–84

[104] Formenti A, Galbiati M and Passoni M 2022 Modeling and simulations of ultra-intense laser-driven bremsstrahlung with double-layer targets *Plasma Phys. Control. Fusion* **64** 044009

[105] Mirani F, Calzolari D, Formenti A and Passoni M 2021 Superintense laser-driven photon activation analysis *Commun. Phys.* **4** 2

[106] Galbiati M, Formenti A, Grech M and Passoni M 2023 Numerical investigation of non-linear inverse compton scattering in double-layer targets *Front. Phys.* **11** 43

[107] Batani D *et al* 2010 Effects of laser prepulse on proton generation *Nucl. Instrum. Methods Phys. Res. A* **620** 76–82

[108] Kaluza M, Schreiber J, Santala M I K, Tsakiris G D, Eidmann K, Meyer-Ter-Vehn J and Witte K J 2004 Influence of the laser prepulse on proton acceleration in thin-foil experiments *Phys. Rev. Lett.* **93** 045003-1-045003-4

[109] Ceccotti T, Lévy A, Popescu H, Réau F, D'Oliveira P, Monot P, Geindre J P, Lefebvre E and Martin P 2007 Proton acceleration with high-intensity ultrahigh-contrast laser pulses *Phys. Rev. Lett.* **99** 185002

[110] Esirkepov T Z *et al* 2014 Prepulse and amplified spontaneous emission effects on the interaction of a petawatt class laser with thin solid targets *Nucl. Instrum. Methods Phys. Res. A* **745** 150–63

[111] Le Garrec B *et al* 2017 Design update and recent results of the Apollon 10 pw facility vol 10238 (SPIE)

[112] Burdonov K *et al* 2021 Characterization and performance of the Apollon short-focal-area facility following its commissioning at 1 pw level *Matter Radiat. Extremes* **6** 138

[113] Ferrari A and Robertson J 2000 Interpretation of Raman spectra of disordered and amorphous carbon *Phys. Rev. B* **61** 14095–107

[114] Daido H, Nishiuchi M and Pirozhkov A S 2012 Review of laser-driven ion sources and their applications *Rep. Prog. Phys.* **75** 056401

[115] Allison J *et al* 2016 Recent developments in geant4 *Nucl. Instrum. Methods Phys. Res. A* **835** 186–225

[116] Mirani F, Maffini A and Passoni M 2023 Laser-driven neutron generation with near-critical targets and application to materials characterization *Phys. Rev. Appl.* **19** 044020

[117] Yogo A *et al* 2023 Laser-driven neutron generation realizing single-shot resonance spectroscopy *Phys. Rev. X* **13** 11

[118] Zimmer M, Rösch T F, Scheuren S, Seupel T, Jäger T, Kohl J, Hofmann D, Schaumann G and Roth M 2024 Assessing the potential of upcoming laser-driven neutron sources and their practical applications for industry and society *Eur. Phys. J. Plus* **139** 5

[119] Stuhl L *et al* 2025 Continuous high-yield fast neutron generation with few-cycle laser pulses at 10 Hz for applications *Phys. Rev. Res.* **7** 137

[120] Marchese N, Cannuli A, Caccamo M T and Pace C 2017 New generation non-stationary portable neutron generators for biophysical applications of neutron activation analysis *Biochim. Biophys. Acta* **1861** 3661–70

[121] Tayyab M, Bagchi S, Moorti A and Chakera J A 2019 Experimental investigation on nuclear reactions using a laser-accelerated proton and deuteron beam *Plasma Phys. Control. Fusion* **61** 115007

[122] Peñas J *et al* 2024 Production of carbon-11 for pet preclinical imaging using a high-repetition rate laser-driven proton source *Sci. Rep.* **14** 11448

[123] Giammarile F *et al* 2024 Production and regulatory issues for theranostics *Lancet Oncol.* **25** e260–9

[124] Spencer I *et al* 2001 Laser generation of proton beams for the production of short-lived positron emitting radioisotopes *Nucl. Instrum. Methods Phys. Res. B* **183** 449–58

[125] Amato E, Italiano A, Margarone D, Pagano B, Baldari S and Korn G 2016 Future laser-accelerated proton beams at ELI-Beamlines as potential source of positron emitters for PET *J. Instrum.* **11** C04007

[126] Rodrigues M R D *et al* 2024 Radioisotope production using lasers: from basic science to applications *Matter Radiat. Extremes* **9** 909

[127] Batani K L *et al* 2025 Generation of radioisotopes for medical applications using high-repetition, high-intensity lasers *High Power Laser Sci. Eng.* **13** 92

[128] Lacoste C L C, Carriére T, Larreur H, Batani D, Raffestin D, Antici P, D'Humiéres E, Nicolaï P and Bardon M 2025 Enhanced laser-driven radioisotope production using a helical coil target with tube *Phys. Rev. Accel. Beams* **28** 093401

[129] Ziegler J F, Ziegler M D and Biersack J P 2010 SRIM–the stopping and range of ions in matter (2010) *Nucl. Instrum. Methods Phys. Res. B* **268** 1818–23

[130] Ishii K and Morita S 1988 Theoretical estimation of PIXE detection limits *Nucl. Instrum. Methods Phys. Res. B* **34** 209–16

[131] Annegarn H J, Zucchiatti A, Sellschop J P F and Booth-Jones P 1987 Pixe characterization of airborne dust in the mining environment *Nucl. Instrum. Methods Phys. Res. B* **22** 325–30

[132] Félix P M, Almeida S M, Pinheiro T, Sousa J, Franco C and Wolterbeek H T 2013 Assessment of exposure to metals in lead processing industries *Int. J. Hyg. Environ. Health* **216** 17–24

[133] Lucarelli F *et al* 2015 The role of pixe in the airuse project "testing and development of air quality mitigation measures in southern Europe *Nucl. Instrum. Methods Phys. Res. B* **363** 92–98

[134] Calligaro T 2008 PIXE in the study of archaeological and historical glass *X-ray Spectrom.* **37** 169–77

[135] Rizzutto M A, Moro M V, Silva T F, Trindade G F, Added N, Tabacniks M H, Kajiya E M, Campos P H V, Magalhäes A G and Barbosa M 2014 External-PIXE analysis for the study of pigments from a painting from the Museum of Contemporary Art *Nucl. Instrum. Methods Phys. Res. B* **332** 411–4

[136] Dran J-C, Salomon J, Calligaro T and Walter P 2004 Ion beam analysis of art works: 14 years of use in the Louvre *Nucl. Instrum. Methods Phys. Res. B* **219–220** 7–15

[137] Massi M, Giuntini L, Chiari M, Gelli N and Mandó P 2002 The external beam microprobe facility in Florence: set-up and performance *Nucl. Instrum. Methods Phys. Res. B* **190** 276–82

[138] Vadrucci M, Bazzano G, Borgognoni F, Chiari M, Mazzinghi A, Picardi L, Ronsivalle C, Ruberto C and Taccetti F 2017 A new small-footprint external-beam PIXE facility for cultural heritage applications using pulsed proton beams *Nucl. Instrum. Methods Phys. Res. B* **406** 314–7

[139] Mirani F *et al* 2021 Integrated quantitative PIXE analysis and EDX spectroscopy using a laser-driven particle source *Sci. Adv.* **7** 60

[140] Passoni M, Fedeli L and Mirani F 2019 Superintense laser-driven ion beam analysis *Sci. Rep.* **9** 9202

[141] Puyuelo-Valdes P, Vallieres S, Salvadori M, Fourmaux S, Payeur S, Kieffer J-C, Hannachi F and Antici P 2021 Combined laser-based x-ray fluorescence and particle-induced x-ray emission for versatile multi-element analysis *Sci. Rep.* **11** 9998

[142] Catrix E, Boivin F, Langlois K, Valliéres S, Boynukara C Y, Fourmaux S and Antici P 2023 Stable high repetition-rate laser-driven proton beam production for multidisciplinary applications on the advanced laser light source ion beamline *Rev. Sci. Instrum.* **94** 103003

[143] Boivin F, Vallieres S, Fourmaux S, Payeur S and Antici P 2022 Quantitative laser-based x-ray fluorescence and particle-induced x-ray emission *New J. Phys.* **24** 053018
[144] Morabito A, Scisció M, Veltri S, Migliorati M and Antici P 2019 Design and optimization of a laser-PIXE beamline for material science applications *Laser Part. Beams* **37** 354–63
[145] Salvadori M, Brandi F, Labate L, Baffigi F, Fulgentini L, Galizia P, Koester P, Palla D, Sciti D and Gizzi L A 2024 Quantitative elemental analysis of a specimen in air via external beam laser-driven particle-induced x-ray emission with a compact proton source *Phys. Rev. Appl.* **21** 064020
[146] Barberio M, Veltri S, Scisció M and Antici P 2017 Laser-accelerated proton beams as diagnostics for cultural heritage *Sci. Rep.* **7** 40415
[147] Romano F P, Caliri C, Cosentino L, Gammino S, Mascali D, Pappalardo L, Rizzo F, Scharf O and Santos H C 2016 Micro x-ray fluorescence imaging in a tabletop full field-x-ray fluorescence instrument and in a full field-particle induced x-ray emission end station *Anal. Chem.* **88** 9873–80
[148] Łach B, Fiutowski T, del Hoyo-Meléndez J M, Koperny S, Krupska-Wolas P, Mindur B, Wiacek P, Wróbel P M and Dabrowski W 2025 Application of a full-field macro-XRF imaging spectrometer to non-invasive investigation of elemental composition in three-dimensional artworks *npj Herit. Sci.* **13** 58
[149] Bjeoumikhov A, Buzanich G, Langhoff N, Ordavo I, Radtke M, Reinholz U, Riesemeier H, Scharf O, Soltau H and Wedell R 2012 The SLcam: a full-field energy dispersive x-ray camera *J. Instrum.* **7** 418–26
[150] Hanf D, Buchriegler J, Renno A D, Merchel S, Munnik F, Ziegenrücker R, Scharf O, Nowak S H and Borany J V 2016 A new particle-induced x-ray emission set-up for laterally resolved analysis over wide areas *Nucl. Instrum. Methods Phys. Res. B* **377** 17–24
[151] Henke B L, Gullikson E M and Davis J C 1993 X-ray interactions: photoabsorption, scattering, transmission and reflection at e = 50-30,000 ev, z = 1-92 *At. Data Nucl. Data Tables* **54** 181–342
[152] Depierreux S *et al* 2009 Laser smoothing and imprint reduction with a foam layer in the multikilojoule regime *Phys. Rev. Lett.* **102** 195005
[153] Cipriani M, Gus'kov S Y, Consoli F, De Angelis R, Rupasov A A, Andreoli P L, Cristofari G, Di Giorgio G and Salvadori M 2021 Time-dependent measurement of high-power laser light reflection by low-z foam plasma *High Power Laser Sci. Eng.* **9** e40
[154] De Angelis R *et al* 2015 Laser-ablated loading of solid target through foams of overcritical density *Phys. Plasmas* **22** 072701
[155] Hohenberger M *et al* 2020 Integrated performance of large HDC-capsule implosions on the national ignition facility *Phys. Plasmas* **27** 112704
[156] Lafon M *et al* 2015 Direct-drive-ignition designs with mid-z ablators *Phys. Plasmas* **22** 032703
[157] Margarone D *et al* 2022 In-target proton-boron nuclear fusion using a pw-class laser *Appl. Sci.* **12** 1444
[158] Tosca M *et al* 2023 Plasma polymers as targets for laser-driven proton-boron fusion *Front. Phys.* **11** 1227140
[159] Picciotto A *et al* 2024 Ammonia borane-based targets for new developments in laser-driven proton boron fusion *Appl. Surf. Sci.* **672** 160797
[160] Turcu I C E, Margarone D, Giuffrida L, Picciotto A, Spindloe C, Robinson A P L and Batani D 2024 Borane (b m h n), hydrogen rich, proton boron fusion fuel materials for high yield laser-driven alpha sources *J. Instrum.* **19** C03065
[161] Molloy D P *et al* 2025 Alpha particle production from novel targets via laser-driven proton-boron fusion *Phys. Rev. Res.* **7** 013230
[162] Ribeyre X, Capdessus R, Wheeler J, d'Humières E and Mourou G 2022 Multiscale study of high energy attosecond pulse interaction with matter and application to proton-boron fusion *Sci. Rep.* **12** 4665
[163] Istokskaia V *et al* 2023 A multi-mev alpha particle source via proton-boron fusion driven by a 10-gw tabletop laser *Commun. Phys.* **6** 27
[164] Meschini S, Laviano F, Ledda F, Pettinari D, Testoni R, Torsello D and Panella B 2023 Review of commercial nuclear fusion projects *Front. Energy Res.* **11** 1157394
[165] Picciotto A *et al* 2014 Boron-proton nuclear-fusion enhancement induced in boron-doped silicon targets by low-contrast pulsed laser *Phys. Rev. X* **4** 031030
[166] Tran N H, Shtam T, Marchenko Y Y, Konevega A L and Lebedev D 2023 Current state and prospectives for proton boron capture therapy *Biomedicines* **11** 1727
[167] Mazzucconi D, Vavassori D, Dellasega D, Airaghi F M, Agosteo S, Passoni M, Pola A and Bortot D 2023 Proton boron fusion reaction: a novel experimental strategy for cross section investigation *Radiat. Phys. Chem.* **204** 110727
[168] Dzelzainis T *et al* 2010 The taranis laser: A multi-terawatt system for laser-plasma investigations *Laser Part. Beams* **28** 451–61
[169] Maffini A *et al* 2026 DataRepository_PPCF-105455 (available at: https://polimi365-my.sharepoint.com/personal/10277594_polimi_it/_layouts/15/onedrive.aspx?id=%2Fpersonal%2F10277594%5Fpolimi%5Fit%2FDocuments%2FDataRepository%5FPPCF%2D105455&ga=1)